# Digital Clone Testing Platform for the Assessment of SHM Systems under Uncertainty

Ilias N. Giannakeas[1, a)], Z. Sharif Khodaei[1, b)] and M. H. Aliabadi[1, c)]

[1]*Department of Aeronautics, Imperial College London South Kensington Campus, Exhibition Road, SW7 2AZ, London, UK*

[a)]Corresponding author: i.giannakeas19@imperial.ac.uk, [b)]z.sharif-khodaei@imperial.ac.uk, [c)]m.h.aliabadi@imperial.ac.uk

**Keywords**: Bayesian Calibration, Damage Detection, Finite Element Modelling of Lamb Waves, Non-Destructive Inspection, Model Assisted Probability of Detection, Gaussian Process

**Abstract**

The performance of a Structural Health Monitoring (SHM) system can be assessed using Probability of Detection (PoD) curves, which is a common tool for the evaluation of Non-Destructive Testing (NDT) methods. This study presents a novel digital clone platform to quantify and account for uncertainties that can be detrimental to the reliability of a SHM system. Uncertainties relating to experimental measurement noise and Environmental and Operational Conditions (EOC) are considered during the definition of a threshold value that aims at reliably distinguishing between pristine and damaged signals. At the same time, the variability of impact damage characteristics and uncertainties associated with Lamb waves interaction in composites are captured though the Bayesian calibration of a Finite Element (FE) model using experimental observations. The FE model is integrated within the digital clone testing platform to substitute the experimental testing and generate a statistical sample of distributed impact events at different locations on a composite plate and compute the Model Assisted Probability of Detection (MAPOD). This approach allows the estimation of the system's performance under different EOC that can be used during the selection and operation of a specific SHM configuration.

## 1 Introduction

The capability of designing composite materials to achieve target stiffness to weight rations has increased their popularity for application within the aerospace industry [1]. Contrary to traditional metallic materials however, composites are very susceptible to impact damage that can reduce significantly the structure's remaining useful life. Current maintenance strategies in aviation rely on schedule-based inspections for the assessment of the aircraft structural integrity. Traditional NDT methods require access to the inspection area and manual inspection of the structure. Structural Health Monitoring (SHM) systems on the other hand can be permanently mounted or embedded into the structure and provide on-demand damage detections, reducing the time interval between inspections and the required manual intervention [2,3]. Guided wave based SHM systems in particular, utilize a distributed network of piezoelectric transducers and have been proven an effective way to detect damage in composite structures and interrogate the structure over long distances [4]–[6].

Damage detection and localization using remote SHM systems can be more challenging compared to traditional NDT methods due to operational and environmental conditions during maintenance [7]. The industrial adoption of SHM systems depends on the capability to quantify the uncertainties associated with the diagnosis of damage and assess its reliability [8]. Although baseline-free methodologies are available [5, 9], a typical SHM system consists of comparing the current measurements with a baseline response that is considered as pristine or defect free and the extraction of a damage index (DI) to determine the current state of the structure [10]. Among others, the accuracy of a SHM system depends on the configuration of the sensor network, the damage location, environmental noise, measurement limitations and device errors [11]. Many

experimental campaigns have been performed in the literature to assess the accuracy of SHM systems however, large scale experimental campaigns can be unfeasible due to their high cost and the time required [12], [13].

The reliability of the SHM system can be assessed following the guidelines in the Military Handbook MIL-HDBK-1823A [14] that relies on the PoD curve estimation. The guidelines in [14] require the collection of experimental data from multiple specimens, with varying damage sizes and locations. Furthermore, measurements must be collected from different operators to reduce human error. Such requirements are suitable for traditional NDT methodologies on metallic structures however they can be restrictive when studying the detectability of BVID in composites. To ensure independence between observations, different specimens must be used for each impact damage test.

Damage localization is also an important aspect of SHM. Various methodologies have been proposed within the scientific community to perform damage imaging based on guided wave measurements such as the RAPID and the Delay-and-sum imaging methodologies [15], [16]. The capability to correctly localize a damage event can be evaluated using metrics such as the absolute error of localization that can be used to construct probability of localization curves [12]. Although damage localization is an integral aspect of SHM, this study is limited in the assessment of the reliability of a system in terms of damage detectability.

To get meaningful estimations on the performance of the SHM system, the uncertainties affecting its accuracy must be quantified and taken into consideration. In this study the uncertainties considered are grouped into two main categories:

1) Category 1: SHM system operation
   Uncertainties regarding the EOC the structure is subjected to, bonding characteristics and measurement noise can alter the wave propagation characteristics and impair the accurate extraction and computation of damage sensitive features. These effects can influence significantly the signals recorded at the sensing locations and lead to undesirable false-positive or false-negative indications, obscuring the true state of the structure [17].
2) Category 2: Variability in the observed DI
   The second category refers to the variability of the observed DI values due to uncertainties in the physical system. These uncertainties may arise due to fluctuations in the material properties, observation error, initial flaws, differences in the manufacturing process, impact damage characteristics, the complex interaction and scattering of Guided waves with damage in composites etc.[18].

Regarding the uncertainties in category 1, many studies have been conducted to quantify their influence on the ability of the SHM system to output accurate predictions (see e.g. [8], [19] and the references therein). Of paramount importance is the temperature difference between the baseline and the current signals. Various temperature compensation algorithms have been proposed in the literature to account for such variations [20]–[22]. A data driven approach is adopted in this study for the statistical quantification of these uncertainties using experimental measurements collected from multiple composite panels at different EOC. Furthermore, the temperature compensation methodology proposed in [20] is implemented to account for the temperature difference between measurements. A threshold value is then defined based on the computed statistical estimates that accounts for the ability of the SHM system to detect damage.

The uncertainties of the second category refer to the natural variability of the physical model that affects the observed DI values. As outlined in [23] and in [24], the estimation of the PoD using MIL-HDBK-1823A requires the collection of a large dataset from multiple specimens. To alleviate the restriction on the number of experimental tests that is feasible to conduct, many Model Assisted Probability of Detection (MAPOD) methodologies have emerged [12], [18], [24], [25] that implement a computer simulator running a mathematical model, that approximates the system response in a cost-efficient manner. Most computer simulators however are deterministic and cannot treat the variability of a physical model [18], [25]. These uncertainties may have a profound impact on the accuracy of the simulator predictions. Probabilistic methods,

such as Bayesian inference, can provide a rigorous mathematical framework for treating uncertainties and updating prior beliefs as more data become available [11]. Such methodologies address the problem of using Bayesian update to infer the parameters of the simulator that best describe the experiments [26]. Bayesian update has been implemented in the literature for damage identification [27], localization [28] as well as damage size estimation [29], [30]

The aim of this contribution is the development of a Digital Clone Testing Platform for the estimation of the MAPOD considering the uncertainties in the two aforementioned categories. The general overview of the platform is illustrated schematically in Figure 1 while a detailed explanation of each step is provided in the methodology section of the paper. The experimental measurements provide inputs at two points within the proposed framework. First the experimentally observed DIs are combined with the numerical predictions to create the combined dataset for the calibration while measurements under different EOC are used to quantify uncertainties in the threshold definition that is subsequently used to evaluate the detectability of damage. A FE model is developed to simulate Lamb wave propagation and interaction with damage. The FE model constitutes a deterministic numerical representation of the physical system. The uncertainties associated with the physical system are accounted for through the Bayesian calibration of the model's parameters using observations from impacted composite panels [31]. This way, the uncertainty regarding the output of the experiments is propagated to the FE model through the uncertainty of the input parameters [32], [33]. The goal is to train a '*digital clone*' that will reduce the number of the costly experimental campaigns. The combination of numerical and experimental observations will offer a more realistic quantification of the underlying uncertainties. The term digital clone is used here to denote the stochastic representation of the system and the estimated calibration parameters that can be used to generate new observations. It is noted that the purpose of the digital clone is not to solely replicate the interaction of guided waves with damage nor to substitute the experimental tests altogether but rather to represent and propagate the variability in the damage features observed during the experimental testing which can reduce the number of specimens required for the estimation of the PoD and provide invaluable information for the reliability assessment of the SHM system.

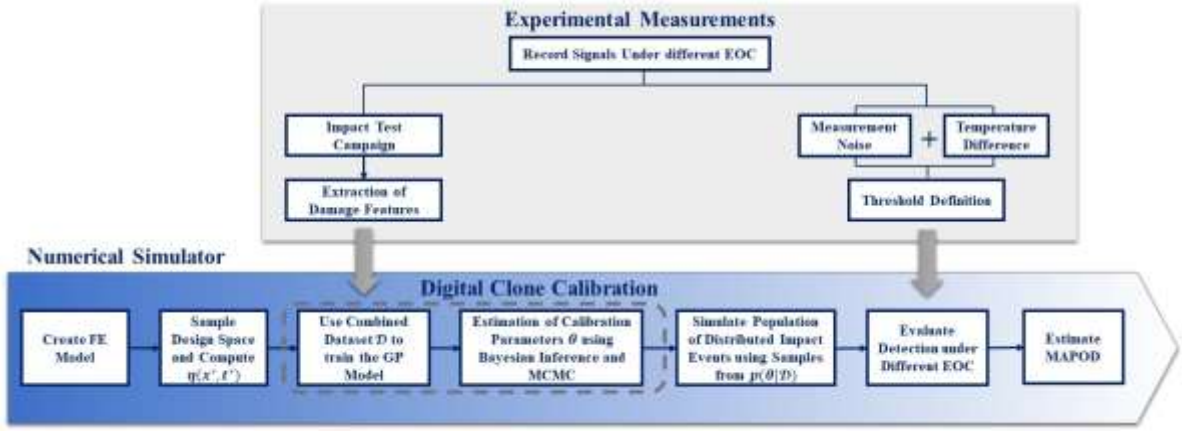


**Figure 1:** Flow diagram of the Digital Clone Testing Platform for the estimation of the MAPOD.

The motivation behind the digital clone platform is to evaluate the reliability of SHM systems for BVID detection under different EOC and address the challenges with the direct estimation of the PoD. Such platform, that considers in a structured framework the identification, quantification and propagation of multiple sources of uncertainty for the estimation of the MAPOD in piezo-sensorized composites, is currently missing from the literature. The Bayesian calibration of the digital clone is based on the method proposed by Kennedy and O'Hagan [31] to leverage the built-in surrogate approximation (Gaussian Process). Information from a single impact location or a single actuation frequency might not be adequate for the estimation of the calibration parameters. This limitation is demonstrated here for the numerical simulator implemented. The Gaussian Process covariance matrix is tailored to allow the incorporation of observations from different impact locations and actuation frequencies, accounting for the characteristics of different wave-modes. This way, the range of the calibration parameters posteriors can be limited. despite the initial use of uninformative priors. Furthermore, the uncertainty in the application of a temperature compensation scheme to reduce the effect of

temperature difference between the current and the baseline measurement is estimated and it is combined with the measurement noise to establish a detection threshold. This results to a threshold value that is temperature dependent, contrary to a constant one that is typically used. The platform developed presents thus a framework to also estimate the temperature range that a given BVID size is detectable. Lastly, the proposed platform is modular. For instance, the definition of the damage sensitive features that are extracted from the signals or the temperature compensation methodology adopted can be modified according to the user's requirements.

This contribution is structured as follows: Section 2 describes the methodology used in this study and contains the experimental configuration used for the data acquisition from composite plates and the calibration procedure of the FE model used. In section 3, the process for the definitions of a threshold value that accounts for the measurement noise and the EOC is defined. Then, in section 4, the experimental observations from the impact test campaign are used to calibrate the FE model and extract the posterior distributions of the model parameters. In section 5, a statistical population of impact events at different locations is generated using the calibrated FE model. The results are combined with the threshold values defined in section 3 to estimate the MAPOD of the SHM system. Lastly, concluding remarks and recommendations for future work are included in section 6.

## 2 Methodology: Development of the Digital Clone Testing Platform

In this section the methodology adopted for the MAPOD estimation is discussed. An overview of the methodology is presented in Figure 1. First the experimental set-up is defined for the impact test campaign and the acquisition of the signals under different EOC. Then the FE model used to simulate guided wave propagation and the calibration approach for the creation of the digital clone is presented.

### 2.1 *Experimental Set-up*

In total, five specimens are used for the acquisition of guided waves measurements before and after the impact events. The plates are made of 12 layers of standard thermoset unidirectional prepreg material M21/194/34%/T800S with stacking sequence $[\pm 45/0_2/90/0]_s$ and thickness $t = 0.184\text{mm}$. The resulting lamina has a total thickness of $t_{lmt} = 2.208\text{mm}$. The lamina is assumed orthotropic and its material properties are given in Table 1.

**Table 1**: Material properties of the unidirectional M21/194/34%/T800S

| $E_{11}$ [GPa] | $E_{22}$ [GPa] | $E_{33}$ [GPa] | $\nu_{12}$ | $\nu_{13}$ | $\nu_{23}$ | $G_{12}$ [GPa] | $G_{13}$ [GPa] | $G_{23}$ [GPa] | $\rho\ \left[\frac{\text{kg}}{\text{m}^3}\right]$ |
|---|---|---|---|---|---|---|---|---|---|
| 141.2 | 8.675 | 8.675 | 0.312 | 0.312 | 0.4 | 4.29 | 4.29 | 3.1 | 1600 |

DuraAct piezoelectric transducers (PZT) are surface mounted for the actuation and the sensing of guided waves in the specimens. The geometry of the plates, the locations of the PZTs and the location of the impact events is illustrated in Figure 2. It is noted that the $0^o$ fibre direction of the composite is oriented along the long side of the plate. The thickness of the PZT wafers is $t_{PZT} = 0.5\text{mm}$, the radius $r_{PZT} = 5\text{mm}$ and they are bonded to the CFRP plate using Hexcel Redux 312 adhesive film.

Due to the dispersive nature of wave propagation in layered composite plates, narrowband excitation is preferred [4]. Here, a 5-tone Hanning windowed input pulse is used for the actuation given as:

$$V(t) = A_0[H(t) - H(t - n/f_c)]\sin(2\pi f_c t)\,(1 - \cos(2\pi f_c t/n))\,, \tag{1}$$

where, $H$ is the Heaviside function, $n$ is the number of cycles in the tone-burst, $f_c$ is the central frequency and $A_0$ is the input amplitude. To avoid repeating the measurements for different values of $f_c$ during the experiments, a chirp signal is used instead. The tone-burst response is extracted using the reconstruction procedure described in [34]. The chirp signal is given as:

$$V_{chirp}(t) = A_0\left[H(t) - H\left(t - t_{chirp}\right)\right]\sin\left(2\pi\left(f_0 t + \frac{f_1 - f_0}{t_{chirp}}t^2\right)\right), \quad (2)$$

where, $t_{chirp} = 2 \cdot 10^{-4}$s is the duration of the chirp signal, $f_0 = 10$kHz is the start frequency and $f_1 = 600$kHz is the end frequency.

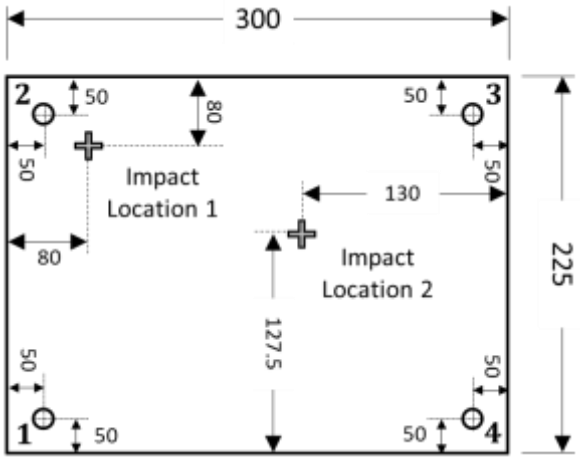


**Figure 2**: Geometry of the composite plates (all dimensions reported in mm). The numbering of the PZTs is indicated at the corners of the plate.

A 12V peak-to-peak amplitude is applied to the actuator PZT using a National Instrument waveform generator while an PXI 5105 Oscilloscope is used to record the signals acquired at the sensor PZTs with a sampling frequency of 60MHz. The total recording duration of the experimental signals is $t_{tot} = 4 \cdot 10^{-4}$s and each measurement is recorded 10 times and averaged to improve the signal to noise ratio.

Pristine measurements are first taken for each plate to establish the pristine baseline $s_{i,j}^{ref}(t)$ where the subscripts $i, j$ are used to denote the actuator and the sensor PZT, respectively [6]. Signals are recorded under different EOC using a TVC J2235 environmental chamber. Pristine measurements are collected from $-5$ ℃ to 55 ℃, with a step of 5 ℃ to generate the dataset of measurements that will be used for the quantification of the uncertainty on the temperature difference. At each step, the temperature is held constant for 20min before guided waves are actuated and recorded. The baseline pristine signals are recorded at reference temperature $T_0 = 25$ ℃.

Subsequently, damage is induced to the plates using an INSTRON CREST 9350 drop tower apparatus with a 20mm hemispherical impactor. After each impact event, the impact location in each plate is inspected with a portable hand-held C-scan camera to evaluate the damage area. In all cases the impact energy level is set as such that induces Barely Visible Impact Damage (BVID) to the plate. Measurements are then taken again to establish the damaged signals, $s_{i,j}(t)$. The impact energy and the resulting damage area for each plate are summarized in Table 2.

**Table 2:** Summary of Impact campaign on the plates.

| Plate Number | Impact Location | Impact Energy [J] | Damage Radius [mm] | Damage Area [mm$^2$] |
|---|---|---|---|---|
| Plate 1 | 1 | 16 | 9.1 | 260.15 |
| Plate 2 | 2 | 14 | 7.5 | 176.71 |
| Plate 3 | 2 | 16 | 8.25 | 213.82 |
| Plate 4 | 2 | 20 | 8.6 | 232.35 |
| Plate 5 | 2 | 20 | 9.0 | 254.47 |

The presence of damage in the plate is evaluated by comparing the pristine with the damaged signals and extracting specific features. These features can be used for the detection, localization and characterization of

damage [16], [35]. Here a DI based on the correlation coefficient is used for the damage detection. The DI is given as [16]:

$$DI(X,Y) = 1 - \frac{C_{XY}}{\sigma_X \sigma_Y}, X = s_{i,j}^{ref}(t) \text{ and } Y = s_{i,j}(t) \quad (3)$$

where, $C_{XY}, \sigma_X$ and $\sigma_Y$ are the covariance and the standard deviations of signals $X$ and $Y$. The correlation coefficient DI detects changes in the shape of the signal that are caused due to the differences in the state of the structure at the time of the data acquisition, compared to the original baseline [35].

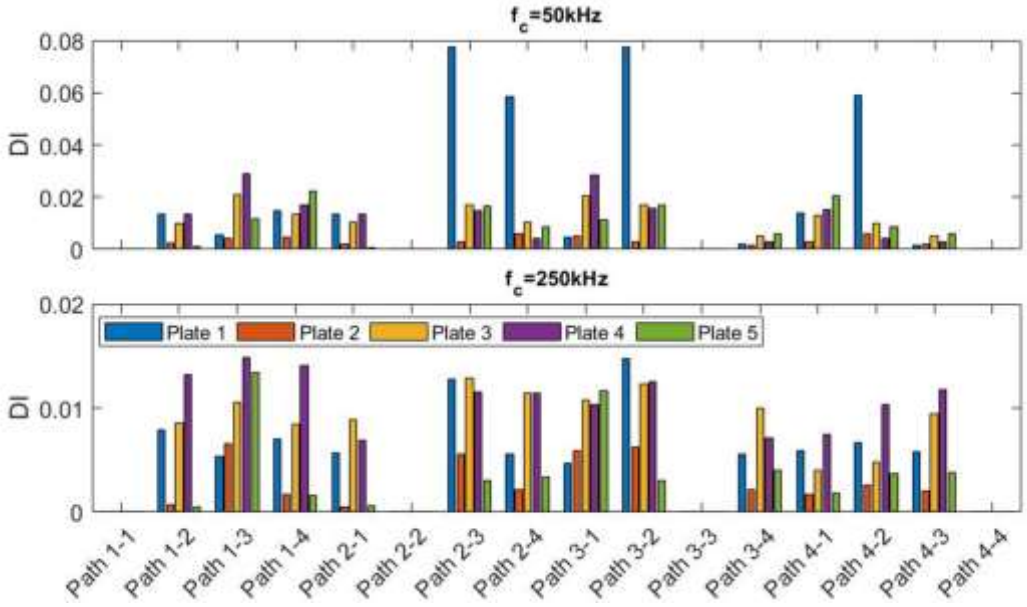


**Figure 3:** Correlation coefficient DI for all PZT pairs used in the plates.

Lamb wave measurements are recorded for the pristine and damaged state for all plates. To record the wave propagation in multiple directions, the measurements are repeated 4 times, each time one PZT acts as the actuator while the others as the sensors. The measurements are stored in a matrix and then, using Eq. (3), the correlation coefficient DI is computed for each actuator-sensor pair. The computed DIs are plotted in Figure 3 for $f_c = 50$kHz and $f_c = 250$kHz. These two frequencies are selected as the former produces clear $A_0$ while the latter $S_0$ wave modes.

The highest values of the DI are observed along wave propagation paths $(2-3), (3-2), (2-4)$ and $(4-2)$ for impact location 1 and paths $(1-3)$ and $(3-1)$ for impact location 2. In [16], a monotonic increase in the correlation coefficient DI is reported for increasing crack lengths. In Figure 3 it is observed that despite Plate 5 having a larger damage area than Plates 3 and 4, the DI along the direct path $(1-3)$ is smaller. Such variabilities in the DIs are expected due to variations during the manufacturing of the composites and the complex nature of the BVID. It is noted that, a path is called the direct path if the perpendicular distance of the impact location to the line segments that connects a pair of PZTs is the smallest among all PZT pairs.

## 2.2 *Calibration of the Computer Simulator*

Modelling of Lamb Wave propagation can be carried out by solving the equation of motion. However, due to material anisotropy and complex geometries in real-life composite structures, analytical solution can be very challenging or impossible [36]. In such cases, the equation of motion can be solved using numerical tools such as the Finite Element (FE) Method [6], [36], [37], Boundary Element Method (BEM) [38], spectral element methods [39], [40], particle models [41], finite differences method [42] and hybrid-semi analytical methods [36], [43].

In this work an FE model developed using the commercial software package Abaqus is used to simulate the actuation, propagation and sensing of guided waves. Time marching can be performed using either an implicit

or an explicit integration algorithm. To ensure the accuracy of the numerical solution, the temporal and spatial discretization must be selected as such that the wave does not propagate further than one wavelength per time step. As noted in [44], the time step must satisfy the Courant-Friedrich-Levy condition in Eq. (4):

$$\delta t \leq \frac{l_e^{min}}{C_g}, \tag{4}$$

where, $\delta t$ is the time-step size, $l_e^{min}$ is the size of the smallest element and $C_g$ is the group velocity. This condition results in step sizes that is comparable to the stability requirement of explicit methods. Given that the intention of the present study is to present a methodology that is computationally applicable to large structures, the Abaqus Explicit solver is used.

The plate is modelled using bi-linear reduced integration shell elements (S4R) while the PZTs with 3D solid elements (C3D8R). The bonding between the PZTs and the plate is assumed perfect and it is enforced through the application of kinematic coupling constraints between the bottom surface of the PZT and the plate [45]. Modelling of the surface mounted PZT actuator is achieved by converting the input voltage from Eq. (1) to an effective displacement that is applied radially on the actuator [46], [47]. Following [47], the effective displacement is $d_{PZT} = Q_A V_{Input}$, where, $Q_A$ is a conversion constant for the actuation. The output voltage of the PZT sensors can be approximated as $V_{Output} = Q_S \varepsilon_{cen}$, where, $Q_S$ is a conversion constant for the sensing and $\varepsilon_{cen}$ is the mean strain at the centre of the PZT wafer. The interested reader is referred to [47] for the computation of $Q_A$ and $Q_S$. The application of the effective radial displacement on the top circumference of the PZT is illustrated schematically in Figure 4 while the amplitude and the frequency content of the input signal is plotted in Figure 5.

The numerical simulations are conducted for the tone-burst signal given in Eq. (1) with i) $f_c = 50\text{kHz}$ ($A_0$ wavemode dominant) and ii) $f_c = 250\text{kHz}$ ($S_0$ wavemode dominant). Each tone-burst signal is simulated individually instead of using the chirp signal with the reconstruction process used during the experimetns. For $f_c = 50\text{kHz}$ the maximum element size is selected as $l_e^{max} = 1\text{mm}$ and the time step equal to $\Delta t = 5.5 \cdot 10^{-8}\text{s}$ while for $f_c = 250\text{kHz}$ the maximum element size is $l_e^{max} = 0.5\text{mm}$ and the time step $\Delta t = 3.5 \cdot 10^{-8}\text{s}$. Based on the experimental time of arrival (ToA) measurements [20], the maximum value of the group velocity is $C_g = 1603\text{m/s}$ and $C_g = 7114\text{m/s}$ for $f_c = 50\text{kHz}$ and $f_c = 250\text{kHz}$, respectively. In the mesh generated, the minimum element size is $l_e^{min} = 0.25\text{mm}$ for both input frequencies and corresponds to the through thickness discretization of the PZT sensor. The above selections satisfy the condition stated in Eq. (4) and provide more than 10 nodes per wavelength that is recommended in [48].

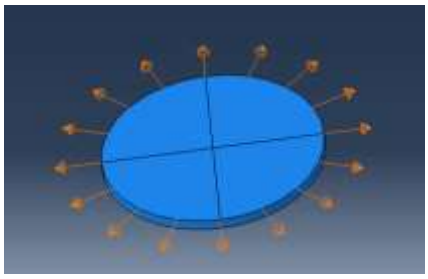

**Figure 4:** Application of the effective radial displacement on the PZT sensor.

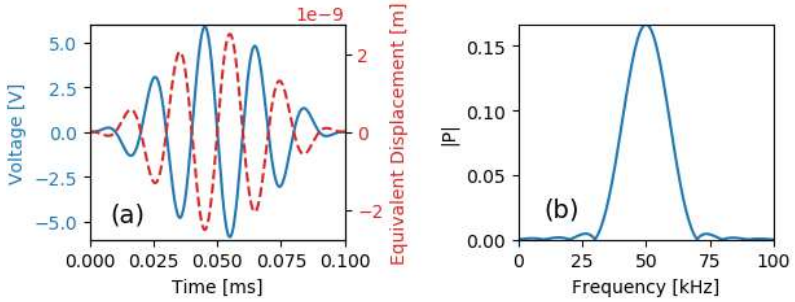


**Figure 5:** Excitation load, a) input voltage and equivalent radial displacement and b) frequency content of the input signal.

In this study, we are interested in simulating Lamb wave propagation and interaction with damage. Despite low velocity impact leading to barely visible indentation on the skin of the structure, typical C-scan and B-scan evaluations of BVID reveal a tapered/conical through thickness damage profile, consisting of a combination of delamination, matrix cracks, fiber breakage, surface buckling etc. [49]. Therefore, to represent the complex nature of different damage profiles, a simplified damage representation is utilized in this work. The material's elastic tensor is given as:

$$C_d = \Delta^{-1}\begin{bmatrix} d_f E_{11}(1-d_m v_{23}v_{32}) & d_f d_m E_{11}(v_{21}+v_{23}v_{31}) & d_f E_{11}(v_{31}+d_m v_{21}v_{32}) & & & \\ & d_m E_{22}(1-d_f v_{13}v_{31}) & d_m E_{22}(v_{32}+d_f v_{12}v_{31}) & & & \\ & & E_{33}(1-d_f d_m v_{21}v_{12}) & & & \\ & & & \Delta d_f d_m G_{12} & & \\ & & & & \Delta d_f d_m G_{23} & \\ & & & & & \Delta d_f d_m G_{13} \end{bmatrix}, \quad (5)$$

where $\Delta = 1 - d_f d_m v_{12}v_{21} - d_m v_{23}v_{32} - d_f v_{13}v_{31} - 2d_f d_m v_{21}v_{32}v_{13}$ and $d_m$ and $d_f$ are the matrix damage and fiber damage, respectively. It is noted that the value 1 indicates pristine material while 0 complete damage. As a simplification, it is assumed that $d_m$ and $d_f$ are uniform through the thickness and with constant values for all elements within the damage radius $d_r$ (Figure 6).

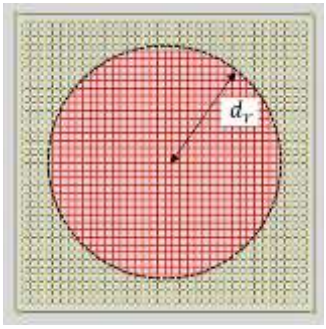


**Figure 6:** Reduction of the material properties for the elements that are located within $r_d$ from the damage location.

Because of the difference between the wave propagation characteristics of the pristine and the damaged material, wave scattering is observed. Each simulation is repeated two times, first no damage is assumed in the plate ($d_m = 1$ and $d_f = 1$) to record the pristine case and then, damage is introduced ($d_m < 1$ and $d_f < 1$) in the elements within $d_r$ to approximate the damaged state. The DI between the signals is then computed using Eq. (3) to evaluate the damage detection capabilities.

The plate geometry from Figure 2 is used to create the numerical model in Abaqus and simulate numerically the Lamb wave propagation and interaction with the damage to perform an initial investigation on the sensitivity of the DI on the value of $d_m$ and $d_f$. Damage is assumed at impact location 2 (see Figure 2) with $d_r = 8\text{mm}$. The damage parameters are varied one at a time and the DI is computed along the direct sensor path 1 – 3, with sensor 1 acting as the actuator. The simulations are repeated for $f_c = 50\text{kHz}$ and $f_c = 250\text{kHz}$.

**Table 3:** Variation of the DI along path 1 – 3 when the damage parameters $d_m$ and $d_f$ are varied to 0.75 and 0.5 one at a time.

| | Computed DI when $d_m$ is reduced to | | Computed DI when $d_f$ is reduced to | |
|---|---|---|---|---|
| | 0.75 | 0.5 | 0.75 | 0.5 |
| $f_c = 50$kHz | 0.0057 | 0.0566 | 0.0098 | 0.0726 |
| $f_c = 250$kHz | 0.0014 | 0.004 | 0.0052 | 0.0358 |

The computed DI for the different values of $d_m$ and $d_f$ is reported in Table 3. It is observed that at both frequencies, the value of the DI is more sensitive to $d_f$ compared to $d_m$. For $f_c = 250$kHz in particular, the sensitivity on $d_f$ is pronounced and significant higher values of DI are observed compared to $d_m$. For BVID, matrix damage is more prominent compared to fiber damage [50] and the value of $d_f$ is expected to be high.

The response of the FE model (computer simulator) depends on the values of $d_r$, $d_m$ and $d_f$. In the proposed setting, $d_r$ is a controlled variable while $d_m$ and $d_f$ are considered model parameters and must be selected as such that are able to capture the experimental observations. The uncertainties associated with model parameters can be constrained by fitting the computer simulator to experimental observations. Such methodologies can implement Monte Carlo or other exploration approaches to train the computer simulator (e.g. [51]).

In their work, Kennedy and O'Hagan [31], developed a methodology for calibration of computer models using a Gaussian process to estimate the simulator output at yet untried values. A Bayesian approach is then implemented to estimate the calibration parameters based on the available experimental observations. The key features of the approach are the introduction of a discrepancy term to account for possible mispatch between the computer simulator and the physical response of the system and the use of a metamodel to reduce the required number of simulator evaluations. Other calibration approaches can be found in the literature such as the contributions in [18], [52], [53] while a review on Bayesian method for damage assessment can be found in [27]. Furthermore, in [26], Bayesian inference is used for the identification of the most probable model in a model class using probability logic. For the sake of completeness, the calibration procedure adopted here is briefly described below.

The aim of the proposed methodology is to calibrate the set of yet unknown calibration parameters $\boldsymbol{\theta}$ using the available experimental observations. From a Bayesian point of view, $\boldsymbol{\theta}$ is treated as a random variable with an associated probability distribution, $p(\boldsymbol{\theta})$ [54] that expresses the prior beliefs on the value of the calibration parameters. The calibration parameters are defined as the vector $\boldsymbol{\theta} = (d_m,\ d_f)$.

Given a dataset of observations $\mathcal{D}$, Bayes theorem states that:

$$p(\boldsymbol{\theta}|\mathcal{D}) = \frac{p(\mathcal{D}|\boldsymbol{\theta})p(\boldsymbol{\theta})}{p(\mathcal{D})}, \tag{6}$$

where, $p(\mathcal{D}|\boldsymbol{\theta})$ is the likelihood of observing dataset $\mathcal{D}$ given a specific choice of calibration parameters, $p(\mathcal{D})$ is the marginal likelihood of observing $\mathcal{D}$ over all possible $\boldsymbol{\theta}$ and $p(\boldsymbol{\theta}|\mathcal{D})$ is the posterior distribution of $\boldsymbol{\theta}$, after observing $\mathcal{D}$ [54]. For the SHM system considered here, the dataset consists of the Damage Index values evaluated for the sensor pair that defines the direct path.

Assume the experiment is repeated $n$ times at input settings $\boldsymbol{x} = (\boldsymbol{x}_1, \boldsymbol{x}_2, \dots, \boldsymbol{x}_n)^T$, resulting in observations $\boldsymbol{y} = \big(y(\boldsymbol{x}_1), y(\boldsymbol{x}_2), \dots, y(\boldsymbol{x}_n)\big)^T$. Following [55], the physical model is described as:

$$y(\boldsymbol{x}_i) = \zeta(\boldsymbol{x}_i) + \varepsilon(\boldsymbol{x}_i), i = 1,2, \dots n \tag{7}$$

where, $\zeta(\boldsymbol{x}_i)$ is the actual response of the physical model, $y(\boldsymbol{x}_i)$ is the observed response of the system, after conducting the experiment, and $\varepsilon(\boldsymbol{x}_i)$ is the observations error. Here it is assumed that the observation error is i.i.d. following a zero-mean Gaussian distribution $N(0, \sigma_\varepsilon)$. The response of the physical system can be

modelled as $\zeta(\boldsymbol{x}_i) = \eta(\boldsymbol{x}_i, \boldsymbol{\theta}) + \zeta(\boldsymbol{x}_i)$ where, $\eta(\boldsymbol{x}_i, \boldsymbol{\theta})$ is the response of the simulator at the true values of the calibration parameters $\boldsymbol{\theta}$ and $\zeta(\boldsymbol{x}_i)$ is a bias term that accounts for the discrepancy between the actual response of the system $\zeta(\boldsymbol{x}_i)$, and the simulator $\eta(\boldsymbol{x}_i, \boldsymbol{\theta})$ [56]. Eq. (7) can then be re-written as:

$$y(\boldsymbol{x}_i) = \eta(\boldsymbol{x}_i, \boldsymbol{\theta}) + \zeta(\boldsymbol{x}_i) + \varepsilon(\boldsymbol{x}_i), i = 1,2, \dots n \tag{8}$$

The term $\zeta(\boldsymbol{x}_i)$ can be used to capture the characteristics of the system that the computer simulator is not able to.

The true values of the calibration parameters $\boldsymbol{\theta}$ are initially unknown to the user. Instead the user can run the simulator $m$ times at pairs $(\boldsymbol{x}_j^*, \boldsymbol{t}_j), j = 1,2, \dots, m$ where $\boldsymbol{x}_j^*$ and $\boldsymbol{t}_j$ are used to denote the simulator input and test values respectively. The simulator results $\eta(\boldsymbol{x}_j^*, \boldsymbol{t}_j)$ are then used to find the values $\boldsymbol{t}$ that fit best the experimental observations. In many cases, the computer simulator might be computationally demanding and unfeasible to run for a large number of $m$. To avoid this restriction and to be able to find the optimum calibration parameters $\boldsymbol{\theta}$, a surrogate model can be implemented to approximate the response of $\eta(\boldsymbol{x}_j^*, \boldsymbol{t}_j)$ for combinations of $(\boldsymbol{x}^*, \boldsymbol{t})$ that the simulator has not been carried out [31], [55], [56]. A Gaussian process (GP) is defined through a mean function $\mu(\boldsymbol{x}, \boldsymbol{t})$ and a covariance function $Cov\big((\boldsymbol{x}, \boldsymbol{t}), (\boldsymbol{x}', \boldsymbol{t}')\big)$ [57]. The simulator is modeled as:

$$\eta(\boldsymbol{x}, \boldsymbol{t}) \sim \mathcal{GP}\big(\mu(\boldsymbol{x}, \boldsymbol{t}), Cov\big((\boldsymbol{x}, \boldsymbol{t}), (\boldsymbol{x}', \boldsymbol{t}')\big)\big). \tag{9}$$

The discrepancy term $\zeta(\boldsymbol{x})$ in Eq. (8) is defined as a zero-mean GP of the form [32]:

$$\zeta(\boldsymbol{x}) \sim \mathcal{GP}(0, Cov(\boldsymbol{x}, \boldsymbol{x}')). \tag{10}$$

The use of a GP for $\zeta(\boldsymbol{x})$ indicates that for a given input $\boldsymbol{x}$ the prior probability for the discrepancy between the simulator and the experiments has a Gaussian distribution centered around zero (i.e. we do not assume that the discrepancy will be either positive or negative) and its variance will be $Cov(\boldsymbol{x}, \boldsymbol{x})$. For further details, the interested reader is referred to the contribution of Brynjarsdóttir and O'Hagan [32] where the meaning and the use of $\zeta(\boldsymbol{x})$ has been discussed extensively.

The matrix containing the pairs of inputs for both the experimental and the numerical observations is defined as $\mathcal{M} = \big((\boldsymbol{x}_1, \boldsymbol{\theta}), \dots, (\boldsymbol{x}_n, \boldsymbol{\theta}), (\boldsymbol{x}_1^*, \boldsymbol{t}_1), \dots, (\boldsymbol{x}_m^*, \boldsymbol{t}_m)\big)^T$ while the vector of $(n + m)$ observations as $\mathcal{D} = \big(y(\boldsymbol{x}_1), \dots, y(\boldsymbol{x}_n), \eta(\boldsymbol{x}_1^*, \boldsymbol{t}_1), \dots, \eta(\boldsymbol{x}_m^*, \boldsymbol{t}_m)\big)^T$. Then the likelihood function can be written as [55], [58]:

$$\mathcal{L}(\mathcal{D}|\boldsymbol{\theta}, \mathcal{Q}) \propto |\boldsymbol{\Sigma}_{\mathcal{D}}|^{-1/2} \exp\big[-0.5(\mathcal{D} - \mu)\boldsymbol{\Sigma}_{\mathcal{D}}^{-1}(\mathcal{D} - \mu)\big] \tag{11}$$

where, $\mathcal{Q} = \{Q_1, Q_2, \dots Q_k\}$ is a set of parameters required for the definition of the GP for the simulator $\eta(\boldsymbol{x}, \boldsymbol{t})$ and the discrepancy $\zeta(\boldsymbol{x}_i)$ and $\boldsymbol{\Sigma}_{\mathcal{D}}$ is the covariance matrix. In the above definitions the only unknowns in the problem are the calibration parameters $\boldsymbol{\theta}$. Following [55], the covariance matrix $\boldsymbol{\Sigma}_{\mathcal{D}}$ is computed as:

$$\boldsymbol{\Sigma}_{\mathcal{D}} = \boldsymbol{\Sigma}_{\eta} + \begin{bmatrix} \boldsymbol{\Sigma}_{\zeta} + \boldsymbol{\Sigma}_{y} & \mathbf{0} \\ \mathbf{0} & \mathbf{0} \end{bmatrix} \tag{12}$$

where $\boldsymbol{\Sigma}_{y}$ is the observation covariance matrix, $\boldsymbol{\Sigma}_{\eta}$ is computed by applying Eq. (9) to the $(n + m)$ input pairs and $\boldsymbol{\Sigma}_{\zeta}$ is computed by applying Eq. (10) to the $n$ inputs of the experimental observations.

Using Eqs. (6) and (11), the posterior distribution of $\boldsymbol{\theta}$ after observing the observation dataset $\mathcal{D}$ is given as:

$$p(\boldsymbol{\theta}, \mathcal{Q}|\mathcal{D}) \propto \mathcal{L}(\mathcal{D}|\boldsymbol{\theta}, \mathcal{Q}) p(\boldsymbol{\theta}) \prod_{i=1}^{q} p(Q_i) \tag{13}$$

where prior distributions have been assigned for the parameters in $\boldsymbol{\theta}$ and $\mathcal{Q}$. The posterior probability will provide updated information on the value of $\boldsymbol{\theta}$, after observing the data $\mathcal{D}$. The posterior probability can be

explored with Monte Carlo approaches [56]. Here, the posterior distribution is explored using the No-U-Turn (NUTS) Hamiltonian Monte Carlo sampler, implemented using PyMC3 package in python [59], [60].

## 3 Threshold value definition

In order to successfully distinguish between pristine and damaged measurements, a threshold value ($Th$) is defined. The purpose of $Th$ is to reliably identify the DIs obtained from a damaged case while its value must be selected such that it provides an adequate statistical confidence for the indications of the SHM system. In this study, it is considered that the baseline and the damaged measurements are taken from the same plate. This reduces the effect of material variability as measurements are not compared between different plates. $Th$ accounts for two main sources of uncertainty: i) the background noise and ii) differences in the EOC between measurements.

External noise that contaminate the signals can be removed though the implementation of appropriate filters. Vibration noise from the structure is typically in the lower frequency range of the structure (<1kHz) inducing an almost constant shape change of the SHM signal while the frequency content of electrical noise and interference with other instruments is usually above 1MHz [8]. The reconstruction process effectively performs a frequency selection process that minimizes the influence of frequencies outside the frequency band of interest [61]. Thus, the influence of the external noise to the measurements is reduced. Furthermore, noise can be further reduced by taking multiple measurements and averaging the signals.

To quantify the measurement noise, 40 pristine measurements are recorded for each of the plates in Table 2. Batches of 10 measurements are randomly generated, averaged and compared between them for each plate. If all measurements were identical, then the DIs between two sets of averaged pristine signals should be 0. Due to the existence of noise, non-zero DI values are computed. The uncertainty between pristine measurements under the same EOC is quantified by using maximum likelihood estimation (MLE) to fit a random variable to the DIs computed from all plates. The random variable is defined as:

$$Th_1(\theta) \sim Gamma\big(a_1(\theta), b_1(\theta)\big) \tag{14}$$

where, $\theta$ is the propagation direction. The DIs computed along path 1-4 ($\theta = 0^o$) are illustrated in Figure 7 (A) while the directional dependency of $Th_1$ is plotted in Figure 7 (B).

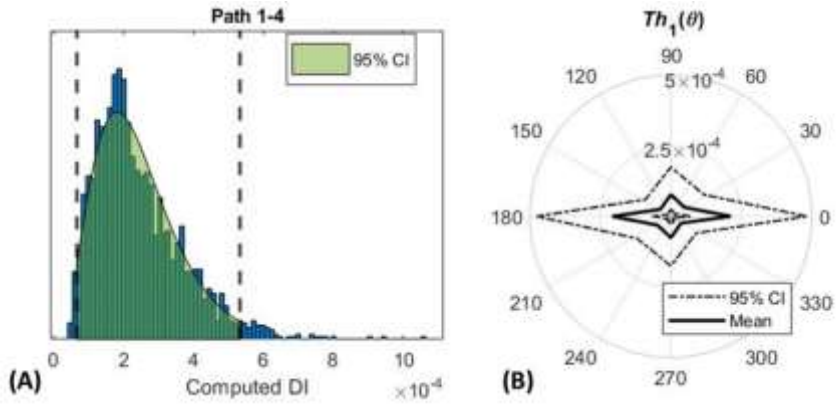


**Figure 7**: (A) Computed DIs along path 1-4 indicating the corresponding 95% confidence interval and (B) directional dependency of $Th_1$.

Comparing the values reported in Figure 3 and Figure 7 it can be seen that the measurement noise computed is approximately two orders of magnitude lower. For simplification, the dependency of $Th_1$ on $\theta$ is dropped by making the conservative approximation $Th_1 = Th_1(0) = Gamma\big(a_1(0), b_1(0)\big)$, where $a_1(0) = 3.909$ and $b_1(0) = 16.18e - 5$.

One of the major sources of uncertainty for SHM systems however stems from the variations in the EOC and in particularly, the temperature at which the measurements have been taken. Many studies have demonstrated

that even small changes in the ambient temperature between the pristine (baseline) and test signal are enough to lead to erroneous decisions regarding the state of the structure, significantly impairing the robustness of the SHM system [17], [20], [62], [63]. Various temperature compensation methodologies have been reported in the literature, both data-driven and physics based, aiming to mitigate the effects of temperature change [17], [64]–[68]. In this study, the data-driven temperature compensation methodology proposed by Yue and Aliabadi [20] is implemented, that has been developed and validated for layered composites with anisotropic behavior.

Two signals that have been recorded at two difference temperatures exhibit variations in their amplitude and shapes due to the temperature dependency of the wave propagation characteristics. The current temperature is denoted with $T = T_0 + \Delta T$, where $T_0$ is the reference temperature and $\Delta T$ is the temperature change. Following [20], the experimental estimation of two factors is suggested, namely $\alpha(\theta, \Delta T)$ and $\beta(\theta, \Delta T)$, to account for the influence of the temperature change on the amplitude and the phase shift of the recorded signals respectively. These factors are estimated as:

$$\alpha(\theta, \Delta T) = \frac{V_{out}(\theta, T)}{V_{out}(\theta, T_0)} \text{ and } \beta(\theta, \Delta T) = \frac{TOA(\theta, T)}{TOA(\theta, T_0)} \tag{15}$$

where, $V_{out}(\theta, T)$ is the amplitude and $TOA(\theta, T)$ is the time of arrival of the received signal. The temperature compensated signal is then computed as:

$$S'(t, T_0, \Delta T) \approx \alpha(\theta, \Delta T) S(\beta(\theta, \Delta T) t, T_0 + \Delta T). \tag{16}$$

Following [20], factors $\alpha(\theta, \Delta T)$ and $\beta(\theta, \Delta T)$ are estimated by fitting a cubic polynomial using least squares regression to the experimentally obtained amplitudes and TOA values along different propagation directions, respectively.

The aim of applying the compensation is to allow reduce the uncertainty when comparing baseline signals with measurements taken at different EOC. To evaluate the uncertainty of the compensation scheme, we compute the DI between the original signal measured at $T_0$ and the compensated signal using Eq. (3) as $DI(S(t, T_0), S'(t, T_0, \Delta T))$. The resulting DI values for different $\Delta T$ values are reported in Figure 8 (A). It is observed that the uncertainty increases as $|\Delta T|$ increases while there appears to be symmetry around $\Delta T = 0$. A power law with the form:

$$Th_2(|\Delta T|) = a_2 |\Delta T|^{b_2} \tag{17}$$

is used to fit the experimental observations. A log-log regression is carried out for the simple linear model $y_i = b_2 x_i + a_2' + \varepsilon$, where $y_i = \ln(Th_2(|\Delta T_i|))$, $a_2' = \ln(a_2)$ and $\varepsilon \sim N(0, \sigma^2)$. The best fitted parameters $a_2'$ and $b_2$ are obtained though maximum likelihood estimation and the resulting expected value $\mathbb{E}(y_i | a_2', b_2, \sigma)$ along with the 95% confidence interval is plotted in Figure 8 (B). The fitted model with its 95% confidence interval is also plotted in the untransformed axes in Figure 8 (A), for comparison with the observed data. The estimated parameters of the linear model are $a_2' = -9.9709$ , $b_2 = 2.025$ and $\hat{\sigma}^2 = 0.0712$ where, $\hat{\sigma}^2$ is the mean square error of the residuals.

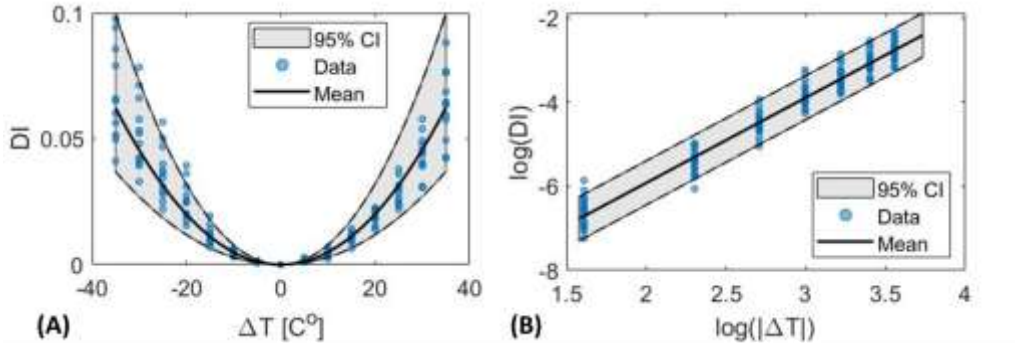


Figure 8: Variation of the threshold uncertainty for different values of $\Delta T$. (A) Original data and (B) transformed for the liner regression fitting.

The final $Th$ value should account for the uncertainty of both the measurement noise and the temperature compensation for the different EOC conditions to reliably distinguish between damaged and pristine measurements. Here we use the value:

$$Th(|\Delta T|) = Th_1^{95\%} + Th_2^{95\%}(|\Delta T|)\,, \tag{18}$$

where the superscripts 95% are used to denote the confidence of the values used. The values in Eq (18) are defined as $Th_1^{95\%} = \{Th_1 : F(Th_1; a_1(0), b_1(0)) = 0.95\} = 5.33 \cdot 10^{-4}$ where $F$ is the Gamma cumulative distribution function and $Th_2^{95\%}(|\Delta T|) = 7.45 \cdot 10^{-5}|\Delta T|^{2.025}$. In the absence of temperature difference between the baseline and the current signal, i.e. $\Delta T = 0$ ℃, the threshold becomes minimum as $Th(0) = Th_1^{95\%} = 5.33 \cdot 10^{-4}$ and takes into consideration the measurement noise only.

## 4 Estimation of the Calibration Parameters

In this section the calibration of the computer simulator is presented. The aim is to introduce an equivalent damage in the numerical model and calibrate the value of the damage parameters $d_m$ and $d_f$ such that the numerically estimated DI values match those obtained through the experimental observations for different damage sizes. It is envisaged that through this process, the numerical simulator will account for uncertainties in the value of the DI relating to the variability of the damage characteristics, manufacturing defects and material strength.

The numerical model is first calibrated for impact damage at locations 1 and 2 where experimental data are available. The steps required for the calibration of the numerical simulator are illustrated schematically in Figure 1. Subsequently, the posterior estimates of the damage parameters are used to draw samples for the creation of the statistical sample of impact events at different locations of the plate. This way, the calibration is first focused on the locations where observations are available. The statistical population is then used to assess the overall performance of the SHM system.

During the experimental campaign, the damage area after each impact event is estimated using C-scan imaging and the equivalent damage radius $d_r$ is computed. Following the definitions from section 2.2, the controlled variables are the damage radius $d_r$ and the frequency of the input signal $f_c$. To take advantage of the higher sensitivity of the DI value on $d_f$ when $f_c = 250$kHz, both frequencies will be considered during the parameter calibration. The controlled variables for the $n$ experimental observations are stored in the input vector $\boldsymbol{x} = (\boldsymbol{x}_1, \boldsymbol{x}_2, \dots, \boldsymbol{x}_n)^T = \left((d_{r,1}, f_{c,1}), (d_{r,2}, f_{c,2}), \dots, (d_{r,n}, f_{c,n})\right)^T$. For each impact location, the DI along each path is computed through Eq. (3). Here, only the direct path is considered for the calibration of the finite element model. Paths 2-4 and 1-3 are considered for impact locations 1 and 2, respectively. Thus, the corresponding observations for each damage location are $\boldsymbol{y} = (y_1, y_2, \dots, y_n)^T = (DI_1, DI_2, \dots, DI_n)^T$, where $n = n_1 = 1$ for impact location 1 and $n = n_2 = 4$ for impact location 2. Using these observations, we estimate the yet unknown calibration parameters $\boldsymbol{\theta} = (d_f, d_m)$.

Two scenarios have been considered: **i**) in the first scenario, only the observations from impact location 2 are considered during the calibration and **ii**) in the second scenario the observations of both impact locations are used simultaneously. The first scenario is used as an example to demonstrate the need of considering both 50kHz and 250kHz measurements during the calibration. The second scenario performs the calibration on all available experimental observations and the distribution of the calibration parameters is extracted that is used in the next section for the computation of the MAPOD.

### **4.1** *Scenario 1*

In this scenario, only the $n_2 = 4$ observations from impact location 2 (plates 2 – 5 from Table 2) are used for the calibration of the finite element model. In order to create the surrogate GP that will substitute the FE simulator $\eta(\boldsymbol{x}_i^*, \boldsymbol{t}_i^*)$ first a sample of possible $(\boldsymbol{x}_i^*, \boldsymbol{t}_i^*) = (d_{r,i}, f_{c,i}, d_{f,i}, d_{m,i})$ pairs needs to be generated that will be used for the training phase. It is assumed that the controlled variable $d_r$ can take the values of $d_{r,i} \in [4\text{mm}, 12\text{mm}]$. From the results in Figure 3 and Table 3, it is expected that the true value of the damage parameters is in the range $d_{m,i}, d_{f,i} \in [0.5,1.0]$. Furthermore, since there are no other information available regarding these parameters, it is assumed that each value within their range is equally probable [54]. To explore the design space more efficiently, samples pairs $(\hat{\boldsymbol{x}}, \hat{\boldsymbol{t}})$ are generated using a Latin Hypercube approach [56], [69], where $\hat{\boldsymbol{x}}$ and $\hat{\boldsymbol{t}}$ are scaled such that $\hat{\boldsymbol{x}}, \hat{\boldsymbol{t}} \in [0,1]$.

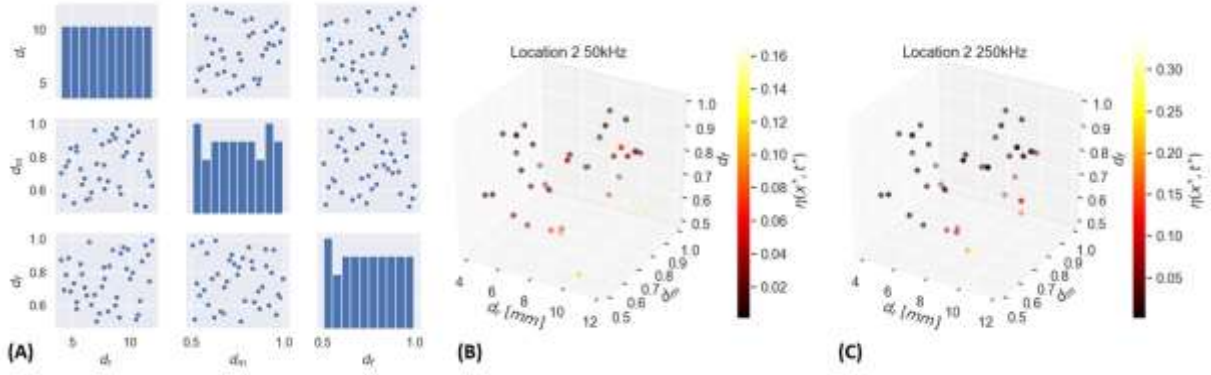


**Figure 9**: (A) Sampled $(\boldsymbol{x}_i^*, \boldsymbol{t}_i^*)$ pairs. (B) Computed DIs for $f_c = 50kHz$. (C) Computed DIs for $f_c = 250kHz$

In total, $m_2 = 40$ samples are taken, and the FE simulation is repeated for each of the sampled pairs. These samples are used to simulate wave propagation for both $f_c = 50kHz$ and $f_c = 250kHz$. The generated samples and the corresponding DI are plotted in Figure 9. As expected, the simulator indicates that the DI value increases as the damage radius $d_r$ increase and the parameters $d_f$ and $d_m$ decrease.

The GP in Eq. (9) is defined by assigning a mean and a covariance function [57]. Following [56], we use a zero-mean function and a squared exponential covariance function. Because for $f_c = 50$kHz the $A_0$ wave mode is dominant while at $f_c = 250$kHz the $S_0$ wave mode is dominant, we treat the two frequencies as independent observations. This is encoded into the covariance function [70] and it is written as:

$$Cov\left((\boldsymbol{x}_i, \boldsymbol{t}_i), (\boldsymbol{x}_j, \boldsymbol{t}_j)\right) = \sigma_\eta^2 \exp\left(-\frac{(d_{r,i} - d_{r,j})^2}{2l_r}\right)\delta\left(f_{c,i}, f_{c,j}\right)\exp\left(-\frac{1}{2}\sum_{1}^{q=2}\frac{(t_{i,q} - t_{j,q})^2}{l_{t,q}}\right) \quad (19)$$

where $q = 2$ as there are two calibration parameters, $\delta(\cdot)$ is the Kronecker delta, $\sigma_\eta^2$ is the variance of the response and $l_r$ and $\boldsymbol{l}_t = [l_{t,1}, l_{t,2}]$ are the length scale parameters that control the smoothness of the function and describe the dependence strength in variations in the $\boldsymbol{x}$ and $\boldsymbol{t}$ values, respectively. The introduction of $\delta\left(f_{c,i}, f_{c,j}\right)$ in Eq. (19) leads to a block diagonal covariance matrix. Similarly, the covariance function of the discrepancy term in Eq. (10) can be computed as:

$$Cov(\boldsymbol{x}_i, \boldsymbol{x}_j) = \sigma_{\eta,\zeta}^2 \exp\left(-\frac{(d_{r,i} - d_{r,j})^2}{2l_{r,\zeta}}\right)\delta\left(f_{c,i}, f_{c,j}\right) \quad (20)$$

Where $\sigma_{\eta,\zeta}^2$ and $l_{r,\zeta}$ are the variance and the length scale for the GP of $\zeta(\boldsymbol{x})$. Denoting $\boldsymbol{l}_r = [l_r, l_{r,\zeta}]$ and $\boldsymbol{\sigma}_\eta = [\sigma_\eta, \sigma_{\eta,\zeta}]$, the posterior distribution from Eq. (13) is written as:

$$p(\boldsymbol{\theta}, \boldsymbol{\sigma}_\eta, \boldsymbol{l}_r, \boldsymbol{l}_t, \boldsymbol{\Sigma}_D|\mathcal{D}) \propto \mathcal{L}(\mathcal{D}|\boldsymbol{\theta}, \boldsymbol{\sigma}_\eta, \boldsymbol{l}_r, \boldsymbol{l}_t, \boldsymbol{\Sigma}_D)p(\boldsymbol{\theta})p(\boldsymbol{\sigma}_\eta)p(\boldsymbol{l}_r)\prod_{i=1}^{q=2} p(l_{t,q}). \quad (21)$$

The following prior distributions are used for the values of $\boldsymbol{\theta}, \boldsymbol{\sigma}_\eta, \boldsymbol{l}_r$ and $l_{t,q}$ [71]:

$$\begin{gathered} p(\boldsymbol{\theta}) \sim Uniform(0.5,1.0) \\ p(\boldsymbol{\sigma}_\eta) \sim HalfCauchy(0.5) \\ p(\boldsymbol{l}_r) \sim HalfCauchy(1) \\ p(l_{t,q}) \sim HalfCauchy(1) \\ p(\sigma_\varepsilon) \sim HalfCauchy(0.02) \end{gathered} \quad (22)$$

In order to explore the posterior distribution, 2 chains with 10000 samples each were sampled. Additionally, 1500 samples were used at the beginning of each chain as burn-in for initialization.

The calibration is carried out first when only the samples with $f_c = 50$kHz are considered and thus the term $\delta\left(f_{c,i}, f_{c,j}\right)$ vanishes in Eq. (19). In this case, $n_2 + m_2 = 44$ observations and pairs of inputs are stored in matrices $\mathcal{D}$ and $\mathcal{M}$, respectively. Since there are two controlled variables and two calibration parameters, $\mathcal{D}$ is a $44 \times 4$ matrix. The posterior distributions of the damage parameters $d_m$ and $d_f$ are plotted in Figure 10.

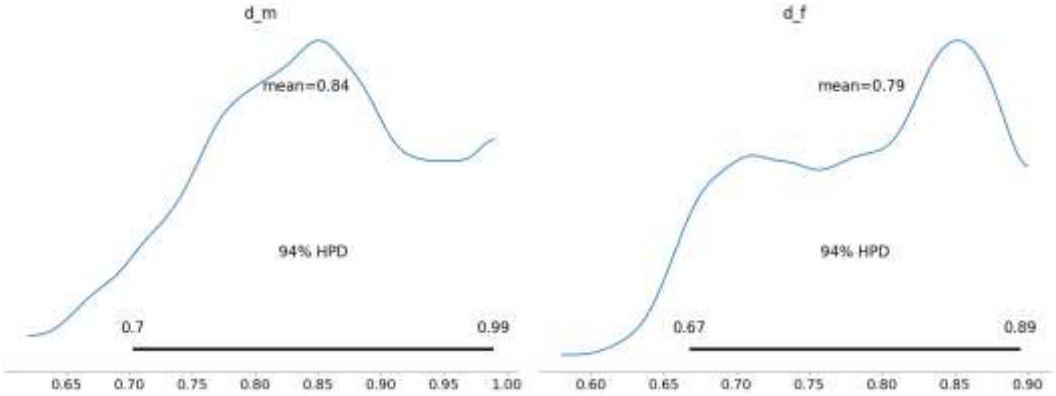


**Figure 10**: Posterior distribution of the damage parameters $d_m$ and $d_f$ when only $f_c = 50$kHz is considered for the calibration.

The calibration is then repeated considering both $f_c = 50$kHz and $f_c = 250$kHz frequencies and the posterior distributions of the damage parameters are plotted in Figure 11. In this case, $2n_2 + 2m_2 = 88$ observations and pairs of inputs are used. When only $f_c = 50$kHz, there are multiple pairs of $d_m$ and $d_f$ values that can be used to fit the experimental observations. Comparing Figure 10 and Figure 11, tighter bounds are obtained for the damage parameters when $f_c = 250$kHz is also observed. This is due to the higher sensitivity of the $S_0$ wave mode on the value of the fiber damage ($d_f$), as discussed in section 2.2.

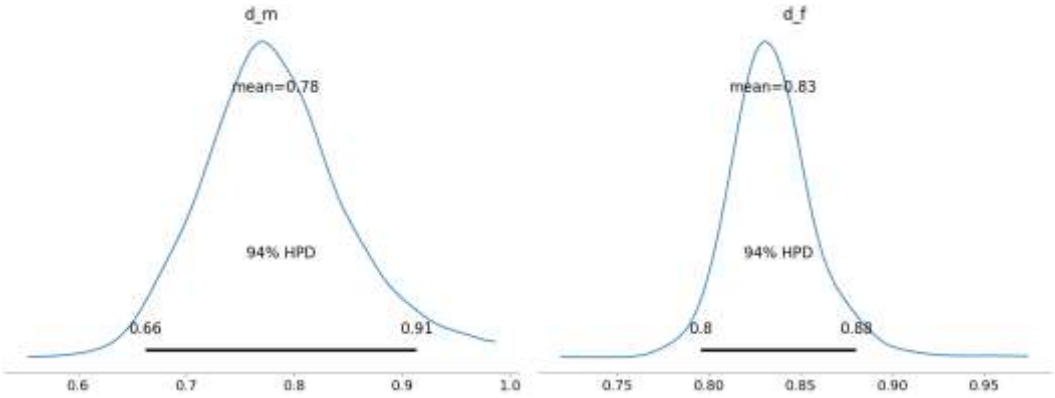


**Figure 11:** Posterior distribution of the damage parameters when both $f_c = 50$kHz and $f_c = 250$kHz frequencies are considered.

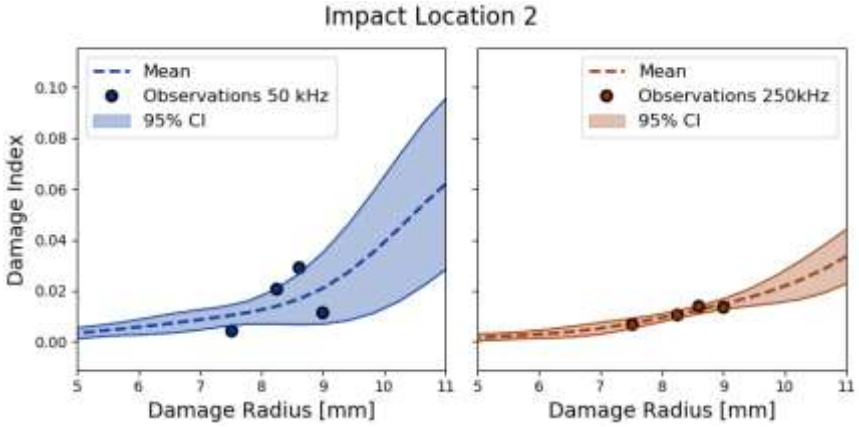


**Figure 12:** Posterior mean estimate of the model prediction with the associated 50% and 95% confidence interval (CI), after the calibration of the simulator.

When both frequencies are considered, the maximum a-posteriori (MAP) estimates are $\bar{d}_m = 0.78$ and $\bar{d}_f = 0.83$ while the 94% highest posterior density (HPD) for each parameter is defined as $[0.66,0.91]$ and $[0.80,0.88]$ for $d_m$ and $d_f$, respectively. The predicted DI is plotted in Figure 12 for $d_r \in [5\text{mm}, 11\text{mm}]$, along with the 95% confidence intervals. Although possible, extrapolation outside this range is not recommended due to the zero mean assumption [72]. Predictions for the DI can be made and explore sensitivities of the model. The variability of the experimental measurements due to uncertainties regarding the damage mechanisms of the BVID is captured in the uncertainty of the damage parameters. Additionally, a higher variability is observed when $f_c = 50$kHz. This can be attributed to different way $A_0$ and $S_0$ wave modes interact with damage [36].

## 4.2 *Scenario 2*

In this scenario, the experimental observations from both impact locations are used simultaneously during the calibration. Additional $m_1 = 38$ samples $(\boldsymbol{x}_i^*, \boldsymbol{t}_i^*)$ are generated and the FE simulator is repeated for damage at impact location 1. Although it would be possible to use the same sample size for both impact locations, the sizes used are different to illustrate the ability of handling heterotopic data [70]. The sampled pairs used, and the estimated DIs for each sample are reported in Figure 13.

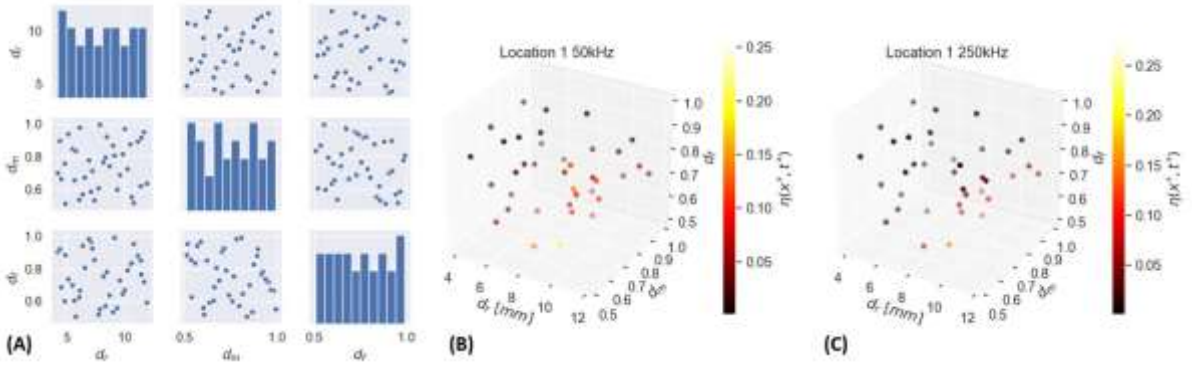


**Figure 13**: (A) Sampled $(\boldsymbol{x}_i^*, \boldsymbol{t}_i^*)$ pairs. (B) Computed DIs for $f_c = 50kHz$. (C) Computed DIs for $f_c = 250kHz$.

An additional variable $k_{loc}$ is introduced as an indicator to distinguish between the different impact locations that takes the value $k_{loc} = 1$ and $k_{loc} = 2$ for locations 1 and 2 respectively. The indicator is concatenated to the input vector as:

$$\boldsymbol{x} = (\boldsymbol{x}_1, \boldsymbol{x}_2, \dots, \boldsymbol{x}_n)^T = \Big(\big(d_{r,1}, f_{c,1}, k_{loc,1}\big), \big(d_{r,2}, f_{c,2}, k_{loc,2}\big), \dots, \big(d_{r,n}, f_{c,n}, k_{loc,n}\big)\Big)^T \tag{23}$$

Due to the introduction of the additional indicator, the covariance function from Eq. (19) is now modified to:

$$\begin{aligned} &Cov\Big((\boldsymbol{x}_i, \boldsymbol{t}_i), (\boldsymbol{x}_j, \boldsymbol{t}_j)\Big) \\ &= \sigma_\eta^2 \exp\left(-\frac{\big(d_{r,i} - d_{r,j}\big)^2}{2l_r}\right) \delta\left(f_{c,i}, f_{c,j}\right) \delta\big(k_{loc,i}, k_{loc,j}\big) \exp\left(-\sum_{1}^{q=2} \frac{\big(t_{i,q} - t_{j,q}\big)^2}{2l_{t,q}}\right) \end{aligned} \tag{24}$$

For impact location 1 there is only a single experimental observation available $(n_1 = 1)$. Since we consider both $f_c = 50$kHz and $f_c = 250$kHz the total number of experimental observations for the simultaneous calibration using both impact locations is $n = 2n_1 + 2n_2 = 10$ observations. Similarly, the number of the available numerical simulations is $m = 2m_1 + 2m_2 = 156$.

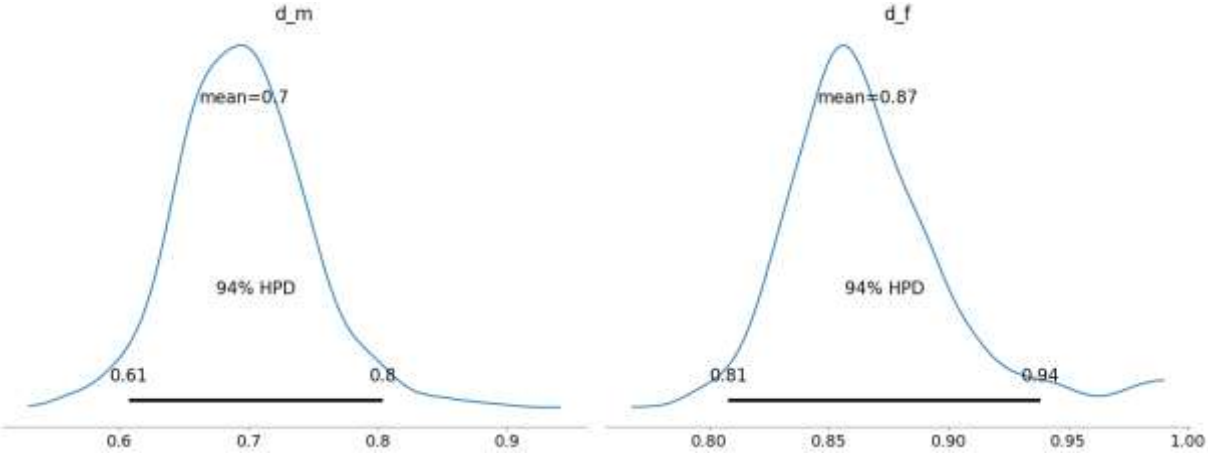


**Figure 14:** Posterior distribution of the damage parameters $d_f$ and $d_m$ when both impact locations are considered for the calibration.

Similar to the previous scenario, 2 chains with 10000 samples each are used to explore the posterior while the same prior distributions as defined in Eq. (22) are used. The resulting posterior distributions of the calibration parameters are illustrated in Figure 14 when both impact locations are considered simultaneously. Furthermore, the predicted DI values for each impact location and actuation frequency are reported in Figure 15. Because in this scenario the calibration parameter is shared between the two impact locations, it is attempted to find the shared value that fits all experimental observations from both impact locations.

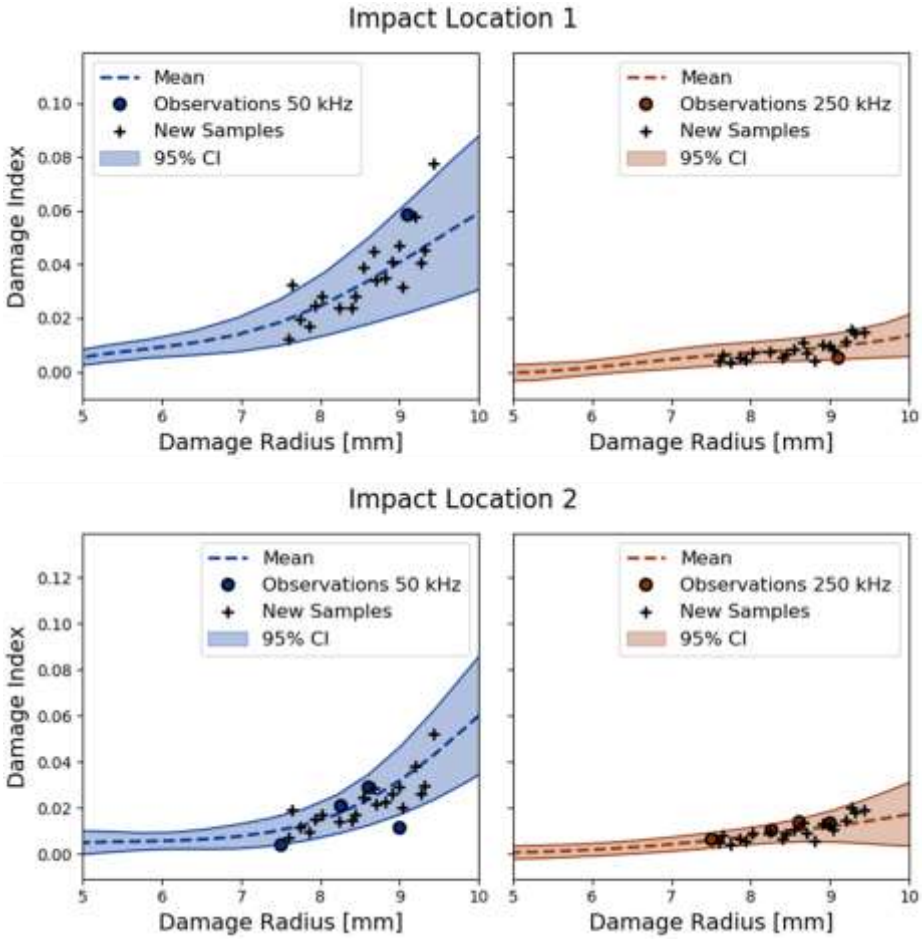


**Figure 15:** Posterior estimate of the model prediction with the 95% prediction bounds when both impact locations are considered.

Comparing Figure 12 and Figure 15 it is evident that there is an upward shift in the posterior prediction of the model after observing the datapoint at impact location 1. It is also noted that the expected value of $d_m$ is smaller than $d_f$, which is expected for BVID damage [50].

**Table 4**: Summary of the computed RMSE values.

| $f_c$ | Experiments | Numerical |
|---|---|---|
| $50kHz$ | 0.01088 | 0.00824 |
| $250kHz$ | 0.00233 | 0.00279 |

For verification, 20 new samples are drawn from the posterior distributions of $d_f$ and $d_m$ and random damage sizes $d_r \in [7.5, 9.5]$mm are assigned to each sample. The simulations are repeated for both impact locations and actuation frequencies. The simulated DIs are reported in Figure 15. This is used to evaluate the capability of the calibrated simulator to be used as a digital clone and generate new samples that can replicate the variability of the experimental observations. The root mean square error (RMSE) is used as a metric for this comparison. For a given frequency, the RMSE is given as:

$$RMSE = \sqrt{n^{-1} \sum (y_i - y_i^*)^2} \tag{25}$$

where $n$ is the number of measurements and $y_i^*$ is the predicted DI of the stochastic model. The experimental measurements and the new numerical samples are then used in $y_i$. The RMSE values computed are summarized in Table 4. For both actuation frequencies, the new numerical samples follow the posterior predictions of the probabilistic model and lead to similar RMSE vales. Thus, new sample points can be generated that follow the variability of the experimental observations.

## 5 Evaluation of the SHM system performance

To estimate the PoD of an impact event it is necessary to evaluate impacts at various locations on the plate. However, gathering experimental measurements at multiple impact locations for different damage severity levels is both costly and time consuming [13]. According to the recommendations in [23], approximately 174 samples from different specimens are required to accurately capture the PoD using hit/miss data. For this reason, it is desirable to substitute experiments with numerical tests.

Following the current guidance in MIL-HDBK-1823 [14], the performance of the SHM system is evaluated based on the minimum damage size ($a$) that can be detected reliably. With $a_{90}$ we denote the damage size that can be detected with 90% probability and with $a_{90/95}$ its upper one-sided confidence interval [2]. In [14], two methodologies are suggested for the computation of the PoD, either using hit/miss data or using the $\hat{a}\ versus\ a$ approach, where $\hat{a}$ denotes the response of the SHM system. The latter method is used here and $\hat{a}$ corresponds to the DI computed using Eq. (3).

The digital clone platform is used to simulate impact damage events at different locations of the plate to generate the required statistical sample to estimate the PoD. In the previous paragraphs, the uncertainties regarding the measurement noise and EOC are accounted for in the threshold value while the uncertainties regarding the observed DI value after an impact event are considered the calibration of the simple FE model with the experimental data. Because the threshold value varies depending on the measurement temperature from Eq (18), the PoD is written as $PoD(a, \Delta T) \approx MAPOD(a, \Delta T) = \Pr[\hat{a} > Th(\Delta T)]$.

In this section, the damage parameters that were calibrated using both impact locations are used to generate numerically a statistical sample of independent impact events at different locations. The inputs for each impact event is defined as a vector $\boldsymbol{b}_i = (x_{loc,i}, y_{loc,i}, d_{r,i}, d_{m,i}, d_{f,i})$ where $x_{loc,i}$ and $y_{loc,i}$ are the $x$ and $y$ coordinates of the $i^{th}$ impact location, respectively. The damage parameters are sampled from the posterior distribution of the calibration process (Figure 14) while $x_{loc,i}, y_{loc,i}$ and $d_{r,i}$ are sampled uniformly in the intervals $20 \leq x_{loc} \leq 280$mm, $20 \leq y_{loc} \leq 205$mm and $3 \leq d_r \leq 18$mm. In total $N_s = 300$ samples are generated. Wave propagation is simulated for each impact event and the DI is computed for each sensor pair. The distribution of the impact events for the numerical testing are presented in Figure 16. These samples are then used to estimate the MAPOD of the SHM system.

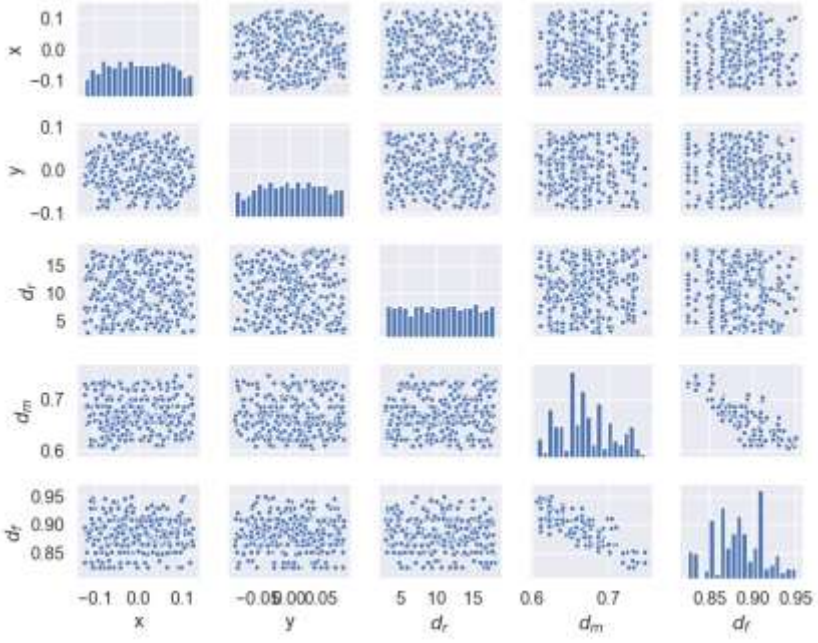


**Figure 16:** Distribution of generated impact events.

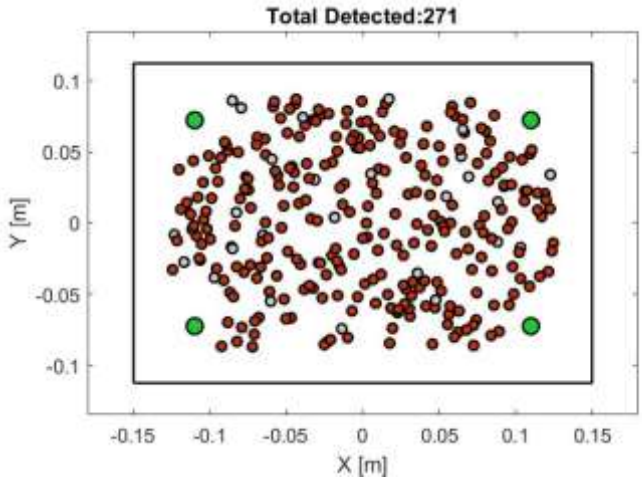


**Figure 17**: Schematic illustration of the detected impact events

Using the results from the numerical simulations, the ability of the SHM system to detect each impact event is evaluated. The resulting DIs can be arranged in a matrix $\widehat{\boldsymbol{A}}$ with dimensions $N_k \times N_s$ where $N_k$ is the number of the sensor pairs. For the SHM network with 4 PZTs considered here, $N_k = 6$ unique paths can be defined while the DIs along repeating paths have been averaged. A Boolean detection matrix $M$ with entries $\mu_{k,l}$ is then used to indicate with $\mu_{k,l} = 1$ if the $l^{th}$ impact event is detected by the $k^{th}$ sensor pair or $\mu_{k,l} = 0$ otherwise. The decision for detection is carried out by comparing the DIs with the threshold value defined in Eq. (18). In Figure 17, green circles represent the locations of the PZT wafers, gray circles the samples with $\mu_\iota = \sum_{k=1}^{N_p} \mu_{k,i} = 0$ (i.e. not detected by any sensor pair) and red circles indicate the samples with $\mu_\iota = \sum_{k=1}^{N_p} \mu_{k,i} \geq 1$ (i.e. detected by at least one sensor pair) when $\Delta T = 0$ in Eq. (18).

The relationship between $a$ and $\hat{a}$ is approximated using a simple linear regression model as [12]:

$$\log(\hat{a}) = \beta_0 + \beta_1 \log(a) + \varepsilon \tag{26}$$

where, $\beta_0$ and $\beta_1$ are the intercept and the slope of the line and $\varepsilon \sim N(0, \tau^2)$ is the error random variable with constant variance. Because the FE model is calibrated along the direct path only, in Eq. (26) $\hat{a}$ corresponds to the DI computed along the direct path and $a$ to the damage radius $d_r$ of the impact event. The prediction bounds of the regression are computed using the Wald method [12], [14]. Then, the PoD is computed as:

$$PoD(a, \Delta T) = \Phi\left(\frac{\log(a) - \hat{\mu}}{\hat{\sigma}}\right) \tag{27}$$

where, $\Phi(\cdot)$ denotes the normal cumulative distribution function. The parameters of $POD$ are related to the linear regression parameters through $\hat{\mu} = (\log(Th(\Delta T)) - \hat{\beta}_0)/\hat{\beta}_1$ and $\hat{\sigma} = \hat{\tau}/\hat{\beta}_1$. The parameters $\hat{\beta}_0$ and $\hat{\beta}_1$ are computed using maximum likelihood estimation while $\hat{\tau}$ is computed through the mean squared error of the regression [2]. Lastly, the covariance matrix of the PoD is computed using the delta method for the definition of the prediction bounds, as outlined in [14]. Other approaches for the estimation of the prediction bounds are available, such as the nonparametric bootstrap method, as discussed in [2].

The DIs obtained from the different impact events are plotted in Figure 18. In the same plot, the mean of the regression and the 95% prediction bounds are also plotted. The estimated regression parameters are $\hat{\beta}_0 = -9.9591$, $\hat{\beta}_1 = 3.2697$ and $\tau^2 = 0.7986$. Using the regression estimates, the PoD can be computed for different values of $\Delta T$. In Figure 19, the estimated PoD is plotted for $\Delta T = 0C^o, \Delta T = 15C^o$ and $\Delta T = 30C^o$ along with the 95% confidence intervals. In each case, the $a_{90/95}$ is also indicated with red dotted lines. Increasing the temperature difference between baseline and the damaged signals not only shifts the PoD curve to higher $a$ values but also increases the 95% prediction bounds. The increased uncertainty associated with differences in the EOC, lead to an increase in the damage size the SHM system can reliably detect.

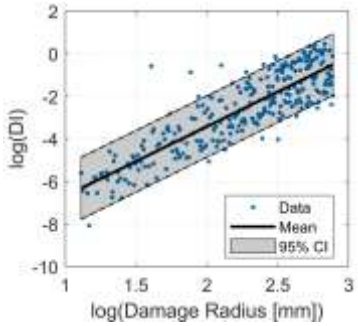


Figure 18:Scatter plot of the DIs simulated using the calibrated FE model and the fitted linear model.

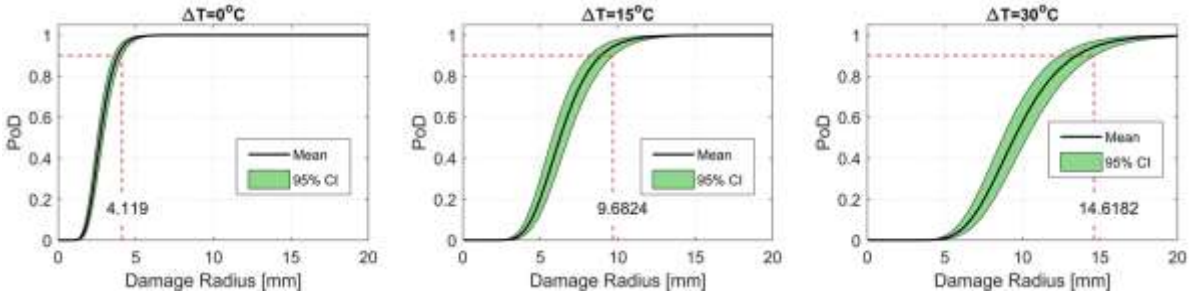


Figure 19: Estimated PoD for $\Delta T = 0C^o, \Delta T = 15C^o$and $\Delta T = 30C^o$. Dotted red lines indicate the $a_{90/95}$ damage size for each case.

The variation of $a_{90/95}$ for different values of $\Delta T$ is illustrated in Figure 20. The results exemplify the need to account the uncertainty associated with EOC and in particular the temperature difference, as it can significantly affect the performance of the SHM system or provide basis for selection between different network set-ups. The combination of model calibration and uncertainty quantification due to measurement noise and EOC provide insights on the performance of the system under different conditions.

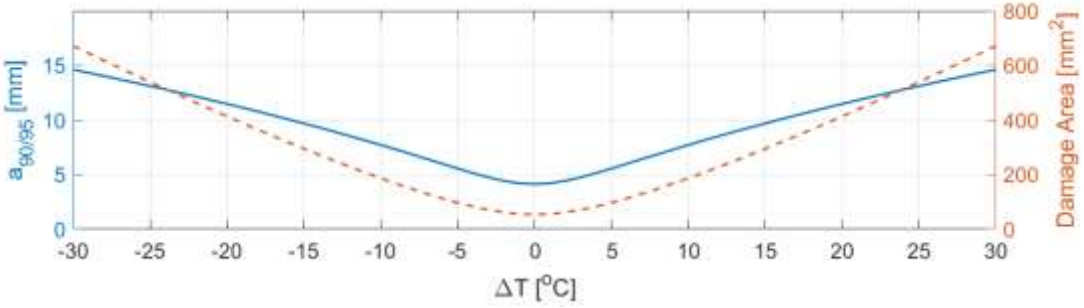


Figure 20: Estimated $a_{90/95}$ for different $\Delta T$ values.

## 6 Conclusions

The accurate computation of the PoD of SHM systems in composites requires many tests that are both costly and time consuming. To address this, a digital clone platform was presented in this study for the estimation of the MAPOD. Uncertainties relating to the reliability of the SHM system were quantified and propagated within the platform to consider different operational conditions and capture the system's response. The variability of the experimental observations was introduced by training a numerical simulator using available experimental data. Because the calibration was carried out within a Bayesian framework, the results can be updated as more observations become available. The platform was then used to generate a statistical sample of impact events for the estimation of the MAPOD under different operational conditions.

The threshold value used for the damage detection was defined through the implementations of a data-driven approach that takes into consideration the measurement noise and differences in the EOC. Despite

implementing a temperature compensation algorithm [20], variations in the temperature between the pristine and the current measurement increases the uncertainty and requires higher threshold values for the reliable distinction between pristine and damaged measurements. Compared to the influence of the temperature difference between the measurements, the measurement noise is less impactful. The threshold value was defined following an exponential relationship to the temperature difference while the measurement noise is added as a constant value, considering the most unfavorable direction of wave propagation.

The, uncertainties relating to the actual geometry of the damage area, the interaction with guided waves and the characteristics of the impact damage were considered through the calibration of a simple FE model. The numerical model was calibrated following the methodology proposed in [31], that allows the combination of numerical results with experimental observations from impacted composite plates while a surrogate model is used to reduce the required number of simulations. This way, the variability of the experimental observations is captured as uncertainty in the input parameters, $d_m$ and $d_f$, of the damage model. Considering the higher sensitivity of the $S_0$ mode on the value of $d_f$, the calibration is carried out at two actuation frequencies $f_c = 50\text{kHz}$ ($A_0$ mode dominant) and $f_c = 250\text{kHz}$ ($S_0$ mode dominant). The posteriors of the damage parameters indicate higher values for matrix damage (i.e. lower $d_m$) compared to the fiber damage, which is expected for BVID in composites.

The calibrated FE model was used in conjunction with the definition of the threshold value to simulate impact events at different locations on the plate and estimate the MAPOD. The PoD of the SHM system is then estimated following the current guidance in MIL-HDBK-1823. The temperature difference between the baseline signal and the current measurement temperature significantly affects the ability of the SHM system to reliably detect an impact damage. This dependency however can be quantified in order to establish temperature ranges that allow the detection of a given impact damage. For instance, using the estimations of this study, the SHM system considered can reliably detect BVID with $200\text{mm}^2$ damage area when $|\Delta T| \leq 10℃$. Thus, taking baseline signals every $20℃$ ensures that $\Delta T$ is never larger that the allowable limits. Such ranges can be used by engineers and managers for the selection and operation of SHM systems.

The FE model used for the simulation of lamb wave interaction with damage assumes that $d_m$ and $d_f$ are uniform through the thickness and are applied in a circular region. Although these assumptions lead to a simplistic model, significant insights can be obtained regarding the performance of the system. The FE model considered can be refined to account for additional damage mechanisms such as delaminations, the complex geometry and the through thickness characteristics of BVID. Such examples can be found in the works of [73], [74]. These models could potentially reduce the number of impact events and impact locations needed to capture the response of the system however, it is important to take into consideration the computational cost of the model and the need to increase the required samples if the unknown parameters are increased.

Furthermore, the framework presented here was used to propagate the variability in the experimental observations to the numerical simulations and estimate the MAPOD. This framework could be modified to generate a sample of impact events for the assessment of the localization capabilities of the SHM system. Then uncertainties relating to damage localization can be propagated to the estimations similar to the work presented in [75] where the case of a through thickness hole in a metallic plate is studied.

As noted in [55], one of the disadvantages of the calibration methodology is that $\boldsymbol{\Sigma}_{\mathcal{D}}$ depends on $\boldsymbol{\theta}$ and thus each time $\boldsymbol{\theta}$ is updated during the Bayesian inference, a determinant and a matrix inversion must be performed which are computationally intensive operations. In the presented applications, the number of available computer simulations and experimental observations is limited, and such restriction should not affect the performance of the methodology. This restriction however is detrimental for applications with high dimensional inputs. The dimensionality of the input matrix however can be reduced using principal component analysis (PCA), as noted in [55].

**Acknowledgements**

The research leading to these results has gratefully received funding from the European JTICleanSky2 program under the Grant Agreement n◦ 945521 (SHERLOC). This project is coordinated by Imperial College London and lead by Leonardo S.p.A. as Topic Manager.

## References

[1] M. Mrazova, "Advanced composite materials of the future in aerospace industry," *Incas Bull.*, vol. 5, no. 3, p. 139, 2013.

[2] C. M. Schubert Kabban, B. M. Greenwell, M. P. DeSimio, and M. M. Derriso, "The probability of detection for structural health monitoring systems: Repeated measures data," *Struct. Health Monit.*, vol. 14, no. 3, pp. 252–264, 2015.

[3] M. Mitra and S. Gopalakrishnan, "Guided wave based structural health monitoring: A review," *Smart Mater. Struct.*, vol. 25, no. 5, p. 053001, 2016.

[4] V. Giurgiutiu, *Structural health monitoring: with piezoelectric wafer active sensors*. Elsevier, 2007.

[5] M. H. Aliabadi and Z. S. Khodaei, *Structural health monitoring for advanced composite structures*, vol. 8. World Scientific, 2017.

[6] Z. Sharif-Khodaei and M. H. Aliabadi, "Assessment of delay-and-sum algorithms for damage detection in aluminium and composite plates," *Smart Mater. Struct.*, vol. 23, no. 7, p. 075007, 2014.

[7] M. S. Salmanpour, Z. Sharif Khodaei, and M. H. Aliabadi, "Impact damage localisation with piezoelectric sensors under operational and environmental conditions," *Sensors*, vol. 17, no. 5, p. 1178, 2017.

[8] P. A. Ochôa, R. M. Groves, and R. Benedictus, "Effects of high-amplitude low-frequency structural vibrations and machinery sound waves on ultrasonic guided wave propagation for health monitoring of composite aircraft primary structures," *J. Sound Vib.*, p. 115289, 2020.

[9] M. S. Salmanpour, Z. S. Khodaei, and M. H. Aliabadi, "Instantaneous baseline damage localization using sensor mapping," *IEEE Sens. J.*, vol. 17, no. 2, pp. 295–301, 2016.

[10] S. Torkamani, S. Roy, M. E. Barkey, E. Sazonov, S. Burkett, and S. Kotru, "A novel damage index for damage identification using guided waves with application in laminated composites," *Smart Mater. Struct.*, vol. 23, no. 9, p. 095015, 2014.

[11] J. M. Karandikar, N. H. Kim, and T. L. Schmitz, "Prediction of remaining useful life for fatigue-damaged structures using Bayesian inference," *Eng. Fract. Mech.*, vol. 96, pp. 588–605, 2012.

[12] J. Moriot, N. Quaegebeur, A. Le Duff, and P. Masson, "A model-based approach for statistical assessment of detection and localization performance of guided wave–based imaging techniques," *Struct. Health Monit.*, vol. 17, no. 6, pp. 1460–1472, 2018.

[13] Z. Sharif-Khodaei, M. Ghajari, and M. H. Aliabadi, "Determination of impact location on composite stiffened panels," *Smart Mater. Struct.*, vol. 21, no. 10, p. 105026, 2012.

[14] M. HDBK, "Nondestructive evaluation system reliability assessment," *Dep. Def. Handb.*, vol. 7, 2009.

[15] J. E. Michaels and T. E. Michaels, "Guided wave signal processing and image fusion for in situ damage localization in plates," *Wave Motion*, vol. 44, no. 6, pp. 482–492, 2007.

[16] X. Zhao *et al.*, "Active health monitoring of an aircraft wing with embedded piezoelectric sensor/actuator network: I. Defect detection, localization and growth monitoring," *Smart Mater. Struct.*, vol. 16, no. 4, p. 1208, 2007.

[17] S. Ahmed and F. Kopsaftopoulos, "Uncertainty quantification of guided waves propagation for active sensing structural health monitoring," presented at the Proceedings of the Vertical Flight Society 75th Annual Forum & Technology Display, Philadelphia, PA, USA, 2019.

[18] O. A. Vanli and S. Jung, “Statistical updating of finite element model with Lamb wave sensing data for damage detection problems,” *Mech. Syst. Signal Process.*, vol. 42, no. 1–2, pp. 137–151, 2014.

[19] N. Yue and M. H. Aliabadi, “Hierarchical approach for uncertainty quantification and reliability assessment of guided wave-based structural health monitoring,” *Struct. Health Monit.*, p. 1475921720940642, 2020.

[20] N. Yue and M. H. Aliabadi, “A scalable data-driven approach to temperature baseline reconstruction for guided wave structural health monitoring of anisotropic carbon-fibre-reinforced polymer structures,” *Struct. Health Monit.*, vol. 19, no. 5, pp. 1487–1506, 2020.

[21] M. Salmanpour, Z. Sharif Khodaei, and M. H. Aliabadi, “Guided wave temperature correction methods in structural health monitoring,” *J. Intell. Mater. Syst. Struct.*, vol. 28, no. 5, pp. 604–618, 2017.

[22] P. Wilcox, A. Croxford, J. Michaels, Y. Lu, and B. Drinkwater, “A comparison of temperature compensation methods for guided wave structural health monitoring,” 2008, vol. 975, no. 1, pp. 1453–1460.

[23] G. Georgiou, “Probability of detection (PoD) curves. Derivation, application and limitations, Jacobi Consulting Limited,” Research Report 454, 2006.

[24] J. C. Aldrin, E. A. Medina, E. A. Lindgren, C. F. Buynak, and J. S. Knopp, “Protocol for reliability assessment of structural health monitoring systems incorporating model-assisted probability of detection (MAPOD) approach,” AIR FORCE RESEARCH LAB WRIGHT-PATTERSON AFB OH MATERIALS AND MANUFACTURING …, 2011.

[25] L. Le Gratiet, B. Iooss, G. Blatman, T. Browne, S. Cordeiro, and B. Goursaud, “Model assisted probability of detection curves: New statistical tools and progressive methodology,” *J. Nondestruct. Eval.*, vol. 36, no. 1, p. 8, 2017.

[26] J. L. Beck, “Bayesian system identification based on probability logic,” *Struct. Control Health Monit.*, vol. 17, no. 7, pp. 825–847, 2010.

[27] Y. Huang, C. Shao, B. Wu, J. L. Beck, and H. Li, “State-of-the-art review on Bayesian inference in structural system identification and damage assessment,” *Adv. Struct. Eng.*, vol. 22, no. 6, pp. 1329–1351, 2019.

[28] M. Zhao, Y. Huang, W. Zhou, and H. Li, “Bayesian uncertainty quantification for guided-wave-based multidamage localization in plate-like structures using Gibbs sampling,” *Struct. Health Monit.*, p. 1475921720979352, 2020.

[29] J. Yang *et al.*, “A probabilistic crack size quantification method using in-situ Lamb wave test and Bayesian updating,” *Mech. Syst. Signal Process.*, vol. 78, pp. 118–133, 2016.

[30] S. He and C.-T. Ng, “Guided wave-based identification of multiple cracks in beams using a Bayesian approach,” *Mech. Syst. Signal Process.*, vol. 84, pp. 324–345, 2017.

[31] M. C. Kennedy and A. O’Hagan, “Bayesian calibration of computer models,” *J. R. Stat. Soc. Ser. B Stat. Methodol.*, vol. 63, no. 3, pp. 425–464, 2001.

[32] J. Brynjarsdóttir and A. O’Hagan, “Learning about physical parameters: The importance of model discrepancy,” *Inverse Probl.*, vol. 30, no. 11, p. 114007, 2014.

[33] D. Xiu, “Fast numerical methods for stochastic computations: a review,” *Commun. Comput. Phys.*, vol. 5, no. 2–4, pp. 242–272, 2009.

[34] J. E. Michaels, S. J. Lee, A. J. Croxford, and P. D. Wilcox, “Chirp excitation of ultrasonic guided waves,” *Ultrasonics*, vol. 53, no. 1, pp. 265–270, 2013.

[35] J. E. Michaels, “Detection, localization and characterization of damage in plates with an in situ array of spatially distributed ultrasonic sensors,” *Smart Mater. Struct.*, vol. 17, no. 3, p. 035035, 2008.

[36] J. L. Rose, “Ultrasonic waves in solid media,” 2000.

[37] Y. Shen and V. Giurgiutiu, "Combined analytical FEM approach for efficient simulation of Lamb wave damage detection," *Ultrasonics*, vol. 69, pp. 116–128, 2016.

[38] Y. Cho, "Estimation of ultrasonic guided wave mode conversion in a plate with thickness variation," *IEEE Trans. Ultrason. Ferroelectr. Freq. Control*, vol. 47, no. 3, pp. 591–603, 2000.

[39] W. Ostachowicz, P. Kudela, M. Krawczuk, and A. Zak, *Guided waves in structures for SHM: the time-domain spectral element method*. John Wiley & Sons, 2011.

[40] P. Kudela, A. Żak, M. Krawczuk, and W. Ostachowicz, "Modelling of wave propagation in composite plates using the time domain spectral element method," *J. Sound Vib.*, vol. 302, no. 4–5, pp. 728–745, 2007.

[41] S. Patra, H. Ahmed, and S. Banerjee, "Peri-elastodynamic simulations of guided ultrasonic waves in plate-like structure with surface mounted PZT," *Sensors*, vol. 18, no. 1, p. 274, 2018.

[42] K. S. Nadella and C. E. Cesnik, "Local interaction simulation approach for modeling wave propagation in composite structures," *CEAS Aeronaut. J.*, vol. 4, no. 1, pp. 35–48, 2013.

[43] H. Mei and V. Giurgiutiu, "Guided wave excitation and propagation in damped composite plates," *Struct. Health Monit.*, vol. 18, no. 3, pp. 690–714, 2019.

[44] S. Duczek, M. Joulaian, A. Düster, and U. Gabbert, "Numerical analysis of Lamb waves using the finite and spectral cell methods," *Int. J. Numer. Methods Eng.*, vol. 99, no. 1, pp. 26–53, 2014.

[45] D. Samaratunga and R. Jha, "Lamb wave propagation simulation in smart composite structures," 2012, pp. 1–11.

[46] C. Yang, L. Ye, Z. Su, and M. Bannister, "Some aspects of numerical simulation for Lamb wave propagation in composite laminates," *Compos. Struct.*, vol. 75, no. 1–4, pp. 267–275, 2006.

[47] Z. Su and L. Ye, *Identification of damage using Lamb waves: from fundamentals to applications*, vol. 48. Springer Science & Business Media, 2009.

[48] D. Alleyne and P. Cawley, "A two-dimensional Fourier transform method for the measurement of propagating multimode signals," *J. Acoust. Soc. Am.*, vol. 89, no. 3, pp. 1159–1168, 1991.

[49] M. Gresil and V. Giurgiutiu, "Guided wave propagation in composite laminates using piezoelectric wafer active sensors," *Aeronaut J*, vol. 117, no. 1196, pp. 971–995, 2013.

[50] B. N. Fedulov and A. N. Fedorenko, "Residual strength estimation of a laminated composite with barely visible impact damage based on topology optimization," *Struct. Multidiscip. Optim.*, pp. 1–19, 2020.

[51] J. Park, S. Ha, and F.-K. Chang, "Monitoring impact events using a system-identification method," *AIAA J.*, vol. 47, no. 9, pp. 2011–2021, 2009.

[52] P. Z. Qian and C. J. Wu, "Bayesian hierarchical modeling for integrating low-accuracy and high-accuracy experiments," *Technometrics*, vol. 50, no. 2, pp. 192–204, 2008.

[53] M. J. Bayarri *et al.*, "A framework for validation of computer models," *Technometrics*, vol. 49, no. 2, pp. 138–154, 2007.

[54] A. Gelman, J. B. Carlin, H. S. Stern, D. B. Dunson, A. Vehtari, and D. B. Rubin, *Bayesian data analysis*. CRC press, 2013.

[55] D. Higdon, J. Gattiker, B. Williams, and M. Rightley, "Computer model calibration using high-dimensional output," *J. Am. Stat. Assoc.*, vol. 103, no. 482, pp. 570–583, 2008.

[56] S. Atamturktur, F. Hemez, and C. Unal, "Calibration under uncertainty for finite element models of masonry monuments," Los Alamos National Lab.(LANL), Los Alamos, NM (United States), 2010.

[57] C. E. Rasmussen, "Gaussian processes in machine learning," 2003, pp. 63–71.

[58] D. Higdon, M. Kennedy, J. C. Cavendish, J. A. Cafeo, and R. D. Ryne, "Combining field data and computer simulations for calibration and prediction," *SIAM J. Sci. Comput.*, vol. 26, no. 2, pp. 448–466, 2004.

[59] M. D. Hoffman and A. Gelman, "The No-U-Turn sampler: adaptively setting path lengths in Hamiltonian Monte Carlo.," *J Mach Learn Res*, vol. 15, no. 1, pp. 1593–1623, 2014.

[60] J. Salvatier, T. V. Wiecki, and C. Fonnesbeck, "Probabilistic programming in Python using PyMC3," *PeerJ Comput. Sci.*, vol. 2, p. e55, 2016.

[61] L. M. Campeiro, R. Z. da Silveira, and F. G. Baptista, "Impedance-based damage detection under noise and vibration effects," *Struct. Health Monit.*, vol. 17, no. 3, pp. 654–667, 2018.

[62] A. J. Croxford, P. D. Wilcox, Y. Lu, J. Michaels, and B. W. Drinkwater, "Quantification of environmental compensation strategies for guided wave structural health monitoring," 2008, vol. 6935, p. 69350H.

[63] Y. Lu and J. E. Michaels, "A methodology for structural health monitoring with diffuse ultrasonic waves in the presence of temperature variations," *Ultrasonics*, vol. 43, no. 9, pp. 717–731, 2005.

[64] C. Fendzi, M. Rebillat, N. Mechbal, M. Guskov, and G. Coffignal, "A data-driven temperature compensation approach for Structural Health Monitoring using Lamb waves," *Struct. Health Monit.*, vol. 15, no. 5, pp. 525–540, 2016.

[65] G. Konstantinidis, B. Drinkwater, and P. Wilcox, "The temperature stability of guided wave structural health monitoring systems," *Smart Mater. Struct.*, vol. 15, no. 4, p. 967, 2006.

[66] J. E. Michaels and T. E. Michaels, "Detection of structural damage from the local temporal coherence of diffuse ultrasonic signals," *IEEE Trans. Ultrason. Ferroelectr. Freq. Control*, vol. 52, no. 10, pp. 1769–1782, 2005.

[67] S. Roy, K. Lonkar, V. Janapati, and F.-K. Chang, "A novel physics-based temperature compensation model for structural health monitoring using ultrasonic guided waves," *Struct. Health Monit.*, vol. 13, no. 3, pp. 321–342, 2014.

[68] A. J. Croxford, J. Moll, P. D. Wilcox, and J. E. Michaels, "Efficient temperature compensation strategies for guided wave structural health monitoring," *Ultrasonics*, vol. 50, no. 4–5, pp. 517–528, 2010.

[69] L. Pronzato and W. G. Müller, "Design of computer experiments: space filling and beyond," *Stat. Comput.*, vol. 22, no. 3, pp. 681–701, 2012.

[70] M. A. Alvarez, L. Rosasco, and N. D. Lawrence, "Kernels for vector-valued functions: A review," *ArXiv Prepr. ArXiv11066251*, 2011.

[71] E. A. Eugene, X. Gao, and A. W. Dowling, "Learning and Optimization with Bayesian Hybrid Models," *ArXiv Prepr. ArXiv191206269*, 2019.

[72] K. P. Murphy, *Machine learning: a probabilistic perspective*. MIT press, 2012.

[73] H. Mei and V. Giurgiutiu, "Wave damage interaction in metals and composites," 2019, vol. 10972, p. 109720O.

[74] A. Migot, Y. Bhuiyan, and V. Giurgiutiu, "Numerical and experimental investigation of damage severity estimation using Lamb wave–based imaging methods," *J. Intell. Mater. Syst. Struct.*, vol. 30, no. 4, pp. 618–635, 2019.

[75] A. Kulakovskyi, O. Mesnil, B. Chapuis, O. d'Almeida, and A. Lhémery, "Statistical analysis of guided wave imaging algorithms performance illustrated by a simple SHM configuration," *J. Nondestruct. Eval. Diagn. Progn. Eng. Syst.*, pp. 1–13, 2021.